

Can We Make Profit by Relocating Batteries?

Profitability Assessment of Spatial-Temporal Arbitrage by Relocatable Battery Energy Storage System

MSc Thesis

Xiangyu Wang



Can We Make Profit by Relocating Batteries?

Profitability Assessment of Spatial-Temporal Arbitrage by Relocatable Battery Energy Storage System

by

Xiangyu Wang

Supervisor TU Delft:
Supervisor Alfen:
Thesis Committee:

Dr. Zian Qin
Ir. René van Wesenbeeck
Dr. Zian Qin
Dr. Hani Vahedi
Dr. Pedro Vergara Barrios

Faculty:
Project Duration:
Student Number:

EEMCS, TU Delft
Feb, 2024 - Aug, 2024
5764890

Abstract

Energy arbitrage is a key activity in privately-owned energy storage system portfolios. However, the profitability of battery energy storage systems in this domain is limited by two primary challenges: the high cost of battery manufacturing and the insufficient temporal volatility of electricity prices within individual bidding area.

In this context, this study explores the economic viability of relocating the utility-scale battery energy storage systems. To enhance profitability, the proposed portable energy storage system integrates a semi-empirical battery degradation model to accurately account for degradation costs, while its mobility allows for travel between different bidding zones to exploit inter-zonal electricity price differences.

A mixed-integer linear programming model is built to optimize the system's daily charging/discharging and transportation scheduling. The system's daily operations within the Norwegian day-ahead market are simulated using a Python model.

The investigation includes comparative analyses to assess how battery location, chemistry, and degradation models influence system profitability. The study compares stationary and portable battery energy storage systems: in the stationary case, it evaluates profitability with different battery chemistries (lithium ferrophosphate and lithium manganese) in different locations, while the portable case explores the impact of different battery chemistries and degradation models (semi-empirical vs. conventional energy throughput).

The findings reveal that none of the stationary energy storage systems can achieve break-even through conventional temporal arbitrage in the Norwegian day-ahead market. In contrast, relocating the battery proves profitable for all four portable energy storage systems.

Additionally, the application of the depth-of-discharge-aware semi-empirical model enhances profitability of portable systems with both battery chemistries, with the lithium manganese system showing a more than 15% increase in investment return rate. This makes lithium manganese a more attractive option than the lithium ferrophosphate battery due to its lower investment cost, shorter payback period, and higher return on investment.

Contents

Abstract	i
Nomenclature	iv
1 Introduction	1
1.1 Electricity Market	1
1.2 Energy Arbitrage	2
1.2.1 Temporal Arbitrage	2
1.2.2 Spatial-Temporal Arbitrage	2
1.3 Research Question	3
1.4 Alfen NV	4
2 Related Work	5
2.1 Temporal Arbitrage Strategy	5
2.2 Spatial-Temporal Arbitrage Strategy: A California Case Study	5
2.3 Battery Degradation	6
2.3.1 Semi-Empirical Cyclic Degradation Model	7
2.3.2 Stress Factor Models	8
2.3.3 Semi-Empirical Calendar Aging Model	10
3 Problem Formulation	11
3.1 System Composition	11
3.2 Model Input: Norwegian Zonal Day-ahead Market Price	12
3.3 Objective Function	14
3.3.1 Objective Function: Arbitrage Revenue	14
3.3.2 Objective Function: Transportation Cost	14
3.3.3 Objective Function: Cyclic Degradation Cost	14
3.3.4 Objective Function: Calendar Degradation Cost	18
3.4 Constraints	19
3.4.1 Constraints: Battery Operation	19
3.4.2 Constraints: Transportation	19
3.4.3 Constraints: Real-time Cycle Counting Algorithm	21
3.5 Simulation	23
3.5.1 Workflow	23
3.5.2 Parameters	24
3.5.3 Price Input Adjustment	25
3.6 Chapter Summary	26
4 Results	27
4.1 Stationary Energy Storage System: LFP Battery	27
4.1.1 LFP: Degradation Comparison	27
4.1.2 LFP: Revenue and Net Present Value Comparison	28
4.2 Stationary Energy Storage System: LMO Battery	29
4.2.1 LMO: Degradation Comparison	29
4.2.2 LMO: Revenue and Net Present Value Comparison	29
4.3 Relocatable Energy Storage System: LFP Battery	31
4.3.1 LFP: Degradation Comparison	31
4.3.2 LFP: Revenue and Net Present Value Comparison	31
4.3.3 LFP: Operational Pattern Comparison	33
4.4 Relocatable Energy Storage System: LMO Battery	35
4.4.1 LMO: Degradation Comparison	35

4.4.2	LMO: Revenue and Net Present Value Comparison	35
4.4.3	LMO: Operational Pattern Comparison	37
4.5	Chapter Summary	38
5	Discussion & Conclusion	39
5.1	Accelerated Cases	39
5.2	Research Questions	41
5.3	Further Discussion: Travel and Charging/Discharging Pattern	42
5.3.1	Long-term Operation Pattern	42
5.3.2	Daily Operation Pattern	44
6	Future Work	46
6.1	Multi-Layer Optimization	46
6.1.1	System Location Planning	46
6.1.2	State of Charge Level	46
6.1.3	SoH Stress Factor	46
6.1.4	Simulation Time Step	46
6.2	Service Portfolios	46
6.3	Price Prediction Error	47
6.4	Grid Impact	47
6.5	Degradation Model	47
6.5.1	Different Stress Factors	47
6.5.2	Cycle Counting Algorithm	48
	References	49
	A Supplemental Results	53
	Acknowledgements	55

Nomenclature

Abbreviations

Abbreviation	Definition
BESS	Battery Energy Storage System
DoD	Depth of Discharge
DSO	Distribution System Operator
ESS	Energy Storage System
EV	Electrical Vehicle
FCR	Frequency Containment Reserve
ISO	Independent System Operator
LFP	Lithium Ferrophosphate
LMO	Lithium Manganese Oxide
LMP	Locational Marginal Price
MILP	Mixed Integer Linear Programming
NMC	Nickel Manganese Cobalt
PESS	Portable Energy Storage System
RES	Renewable Energy Source
SCN	Smart Charging Network
SEI	Solid Electrolyte Interphase
SESS	Stationary Energy Storage System
SoC	State of Charge
SoH	State of Health
TSO	Transmission System Operator

Symbols

Symbol	Definition	Unit
C_{hour}^{cal}	Calendar cost per hour	[€/h]
C^T	Transportation cost per hour	[€/h]
C_{cyc}^{unit}	Cyclic cost per unit energy	[€/MWh]
C_{deg}^{cyc}	Cyclic degradation cost	[€]
C_{deg}^{cal}	Calendar degradation cost	[€]
C^D	Degradation cost	[€]
C^T	Transportation cost	[€]
C^{rep}	Battery replacement cost	[€]
d_{nm}	Transportation time from zone n to m	[h]
E_{eol}	End-of-life energy throughput	[MWh]
E^{PESS}	System energy capacity	[MWh]
f_{sei}	Linearized SEI formation rate	[-]
f_d	Linearized degradation model, general form	[-]
$f_{d,1}$	Linearized degradation rate per cycle	[-]
L_{cal}, L_{cyc}, L	Calendar, cyclic and total degradation	[-]
N	Number of cycle	[-]
$N_{eq,i}$	Equivalent full cycle of the ith cycle	[-]
$N_{life[\delta=\delta_i]}$	Lifetime cycle number at cycle depth δ_i	[-]
$N_{life[\delta=1]}$	Lifetime cycle number at full cycle	[-]
P_n^{chg}, P_n^{dis}	Charging, discharging power in bidding zone n	[MW]
P^{max}	System Power Capacity	[MW]
R	Arbitrage income	[€]
S_δ	Stress factor for cycle depth	[-]
S_σ	Stress factor for average state of charge	[-]
S_T	Stress factor for cell temperature	[-]
Δt	Simulation time step	[h]
T_c	Cell temperature	[°C]
x	Auxiliary state of charge variable	[-]
Z^{chg}, Z^{dis}	Charging and discharging state indicator	[-]
$Z_{st}^{chg}, Z_{st}^{dis}$	Charging and discharging start indicator	[-]
$Z_{end}^{chg}, Z_{end}^{dis}$	Charging and discharging end indicators	[-]
Z^{CC}	End-of-cycle indicator	[-]

Symbol	Definition	Unit
$\alpha_{cal,1,2,3,4}$	Coefficients for calendar degradation model	[-]
α_n, β_n	Binary arrival and departure indicator	[-]
$\alpha_{sei}, \beta_{sei}$	Coefficients for SEI cyclic degradation model	[-]
γ_{nm}	Binary transportation indicator	[-]
δ	Cycle depth	[-]
η	Efficiency of charging/discharging	[-]
θ_n	Binary auxiliary variable	[-]
λ_n	Electricity price in bidding zone n	[€/MWh]
σ	Average state of charge of cycle	[-]
ω_n	Binary location indicator in zone n	[-]

1

Introduction

The impact of global warming is becoming increasingly apparent. Data from the European Union's Copernicus Climate Change Service indicates that, as of February 2024, the global average temperature over the past year was 1.52°C higher compared to the average of the period between 1850 and 1900 [1]. In the Paris Climate Agreement, nearly 200 nations committed to limiting the rise in global average temperature to below 2°C above preindustrial levels, with an aspirational goal of capping it at 1.5°C [2].

Given that 87% of global greenhouse gas emissions originate from energy supply, which is primarily fueled by fossil sources [3], and considering the dramatic increase in fossil fuel consumption over the past half-century, the need for change is evident. By 2022, fossil fuel consumption had surged to 137,237 TWh, which was roughly seven times the amount consumed in 1950 (20,138 TWh) and nearly double the 1980 level (70,620 TWh) [4]. Therefore, transitioning from traditional fossil fuels to renewable energy sources (RES) is essential for sustainable development in the coming decades.

Fortunately, the share of renewable energy in global consumption is increasing as the consensus of sustainable development is gradually reached among scientific researchers, corporations, and private institutions. 2023 had seen a global annual renewable capacity additions increase by almost 50% (nearly 510 GW), which is the fastest growth rate in the past two decades [5]. Currently, approximately one-seventh of the global primary energy is derived from renewable technologies, with significant contributions from hydropower, wind, solar, biomass, and geothermal sources [6].

1.1. Electricity Market

Necessitated by the inherently uncertain, intermittent, and varying nature of renewable energy [7, 8], the rising share of RES is driving an increased demand for energy storage system(ESS). In the absence of ESS, grid malfunctions such as frequency deviations and voltage drops become more challenging to address, thereby imposing significant operational difficulties on the grid.

As grid operators, transmission system operators (TSOs) and distribution system operators (DSOs) are tasked with maintaining the stability and integrity of the power grid. Consequently, these operators need to use the flexibility offered by ESS to manage potential grid incidents. However, according to Article 36 of the Electricity Directive (EU) 2019/944, EU-wide grid operators are generally prohibited from owning, developing, managing, or operating ESS unless specific conditions are met [9].

As a result, market-based methods have become a critical tool for maintaining the normal operation of the power grid. This approach allows ESS owners to maximize their profits by optimizing their portfolios. ESS owners can make profit by participating in electricity trading or receive reimbursement by providing capacity and various ancillary services [10] such as frequency control, voltage control, and reactive power management [11], among others.

1.2. Energy Arbitrage

1.2.1. Temporal Arbitrage

Among all the portfolio options mentioned, energy arbitrage involves utilities purchasing electricity during off-peak hours when prices are the lowest, storing it, and then selling or using the electricity during peak hours when the prices are the highest. Energy arbitrage leverages temporal price differences, and the arbitrage revenue is thus dependent on price volatility.

Studies on the arbitrage profitability of battery energy storage systems (BESS) have been conducted in various global markets. Bradbury et al. [12] had evaluated and compared 14 ESS technologies across seven regional markets in the US, with profitability assessed using the internal rate of return (IRR). The findings indicated that Li-ion batteries were not attractive when compared to other ESS technologies, as their IRR values were below zero in all seven markets, suggesting that BESS investments would not break even. Lin et al. [13] examined BESS participation in the Chinese electricity market, indicating that BESS could achieve positive returns in certain districts with sufficiently large peak/off-peak price differences.

In Europe, Metz et al. [14] conducted an investigation into BESS arbitrage within the German electricity market, concluding that a sevenfold increase in price volatility is necessary for storage to become profitable. Hu et al. [15] employed real market data from key European electricity markets, including those in Germany, Denmark, France and Italy, to assess the potentially profitable utilization time and rate. Their findings suggest that BESS is currently not feasible for energy arbitrage in European electricity markets. Arcos-Vargas et al. [16] looked into the influence of BESS technology on electricity arbitrage in the Iberian market, forecasting that Li-Ion BESS arbitrage will become profitable from 2024 onwards due to improved round-trip efficiency and extended life cycles.

1.2.2. Spatial-Temporal Arbitrage

In the context of temporal arbitrage, BESSs usually remain stationary at a specific location, generating profit by exploiting temporal price differences. However, with the increasing penetration of RES, significant variations in flexibility demand are observed not only over time but also across different geographic locations [17].

Consequently, electricity prices exhibit significant temporal and spatial variations [18]. For example, several Independent System Operators (ISOs) in the US, Canada (Ontario), New Zealand, and Singapore determine the electricity market clearing price for various locations on the transmission grid using locational marginal pricing (LMP), also known as nodal pricing [19] as in Figure 1.1.

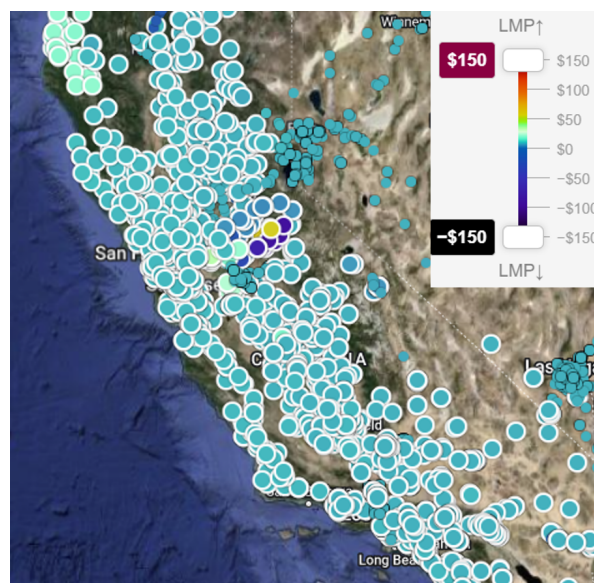


Figure 1.1: The DAM electricity nodal price from CAISO [20] on 05/25/2024 hour: 6-7

Compared to purely temporal arbitrage, fully exploiting spatial-temporal price differences across different locations and times appears to be more profitable. However, this requires that the ESS possesses mobility, making electric vehicles (EVs) a natural fit. To investigate EV arbitrage profitability, Tepe et al. [21] demonstrated that optimizing aggregated EV pools for the provision of frequency containment reserves (FCR) and arbitrage can increase revenue by up to sevenfold. Sarker et al. [22] proposed a centralized model to co-optimize transformer aging and benefits for EV owners, showing that this approach can extend the lifetime of grid assets at the cost of a modest reduction in arbitrage benefits. However, the limited capacity of EV batteries, the uncertain travel routes, and the primary focus on mobility complicate their full utilization as a BESS in arbitrage scenarios and hinder the complete exploitation of spatial-temporal price differences.

The concept of a utility-scale portable energy storage system (PESS) for spatial temporal arbitrage was first introduced by He et al. [23] in a California case study. In this study, a PESS, comprising an electric truck, utility-scale energy storage, and a power converter, travels between different nodes to take advantage of LMP prices in the California day-ahead market (DAM). The findings indicated that mobilizing the ESS could increase its life-cycle revenue by up to 70% in certain areas. Additionally, the life-cycle revenue from spatial-temporal arbitrage could fully cover the PESS cost in regions such as San Diego and San Mateo. The study also revealed that the PESS is more profitable than a stationary energy storage system (SESS) in approximately 36% of the 33 examined counties.

1.3. Research Question

Unlike the LMP adopted in the US, European electricity markets currently employ a zonal pricing model [24]. This model is based on the concept of bidding zones, which are typically treated as single nodes without accounting for internal congestion [25]. Generally, a bidding zone corresponds to an entire country, such as the Netherlands, Belgium, and France. While in Nordic countries like Denmark, Norway, and Sweden, a bidding zone represents a specific large region [26] as in Figure 1.2.

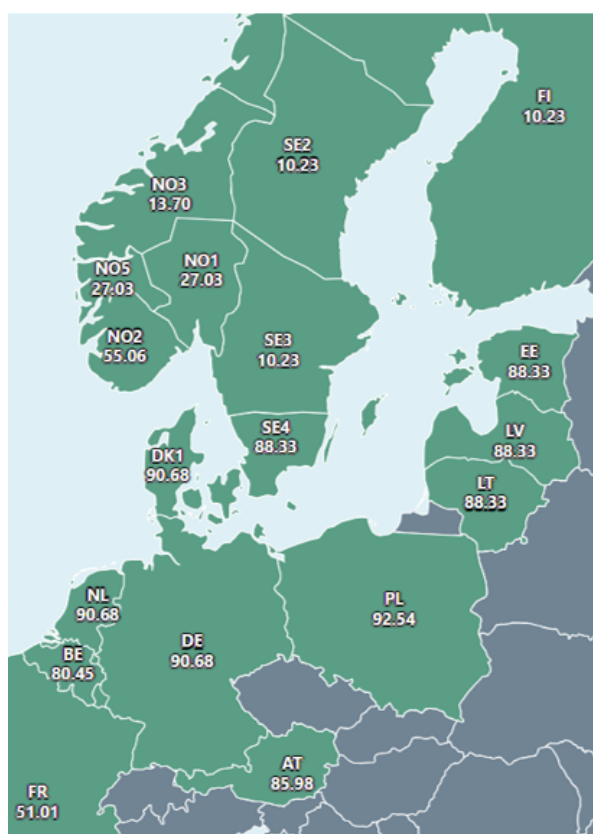


Figure 1.2: The DAM electricity zonal price from NordPool [26] on 05/25/2024 hour: 6-7

Building on the approach in [23], a utility-scale PESS model, comprising E-mobility, BESS, and a power converter, is built to investigate the profitability of spatial-temporal arbitrage across different bidding zones. Unlike the energy throughput degradation model in [23], this thesis integrates the existing spatial-temporal arbitrage decision model with a semi-empirical battery degradation model (discussed in detail in Section 2.4) to account for battery degradation costs during the decision-making phase. This thesis primarily aims to answer the following research questions:

Under the general premise of **considering the semi-empirical battery degradation model**:

- **RQ1:** Is the proposed PESS model profitable in general?
- **RQ2:** Is the proposed PESS model more profitable than SESS model?
- **RQ3:** How will the battery chemistry and degradation model influence the spatial-temporal arbitrage profitability?

1.4. Alfen NV

This thesis is a collaborative project with Alfen NV.

Alfen, originally founded in 1937 as "J. van Alfen's factory of high and low voltage equipment" in Hilversum, has evolved into a pivotal entity within the modern electricity grid. With a portfolio including transformer stations, energy storage systems, and charging stations for EVs, Alfen plays a crucial role in connecting and supporting the electrical infrastructure and is structured into three core divisions: Smart Grids, EV Charging, and Energy Storage.

- **EV Charging:** Alfen's Smart Charging Network (SCN) is at the forefront of charging plaza technology. It functions as an integrated charging network in which each station independently adjusts its charging speed through dynamic load balancing. The SCN system ensures coordinated group operation while allowing individual station control. Alfen now provides comprehensive charging solutions for residential, commercial, and public spaces, featuring products such as the *Eve* series and the *Twin* series.
- **Smart Grids:** Alfen's Smart Grids division specializes in prefabricated transformer stations. Since constructing its first transformer station in the 1960s, Alfen has continually innovated, ensuring that each station is equipped with latest technology and tailor-made solutions to meet the needs of various users and situations.
- **Energy Storage:** Alfen's energy storage solutions are based on two main products: *TheBattery Elements* and *TheBattery Mobile*. The battery containers are tailor-made for different markets and applications, but based on the same design principles to guarantee optimal performance, flexibility, modularity and a long service life.

2

Related Work

Although BESSs are well-suited for energy arbitrage due to their ease of deployment, rapid response, and high efficiency, the economic feasibility of battery arbitrage remains problematic because of the relatively high manufacturing costs. Consequently, developing an optimal arbitrage strategy is crucial for BESS owners to ensure economic viability

2.1. Temporal Arbitrage Strategy

Aiming at maximizing the BESS profit, several studies have been conducted to optimize the operational schemes for temporal arbitrage. Peñaranda et al. [27] developed a mixed-integer linear programming (MILP) model aimed at maximizing economic benefits, quantified by arbitrage income, within the Colombian electricity market. This study incorporates battery degradation approximated through a piece-wise linear model, with the battery state of health being updated iteratively.

In another study, Bai et al. [28] introduced a BESS arbitrage optimization model utilizing an online sliding-window dynamic programming strategy. This approach balances short-term revenue against long-term battery life loss, aiming to maximize long-term profit over an extended time horizon. The profit is defined as the difference between arbitrage revenue and degradation cost, with the degradation cost computed based on a nonlinear aging trajectory.

2.2. Spatial-Temporal Arbitrage Strategy: A California Case Study

He et al. [23] conducted the first case study of spatial-temporal arbitrage utilizing utility-scale PESS. This case study in California, employed a MILP model to maximize daily profit. Several distinctions from previous temporal arbitrage studies were noted:

1. The model's input comprises DAM prices from multiple nodes, rather than a single area.
2. The MILP model contains not only battery operation but also PESS location constraints.
3. The objective function includes a term accounting for the travel cost between different nodes.

In this study, battery degradation is incorporated into the objective function as an 'opportunity cost' term. This formulation implies that while degradation is factored into the optimization, the degradation cost is re-added to the final objective function value to calculate the actual revenue, since the battery cost is fundamentally part of the capital expenditure.

In the objective function, the battery degradation term is quantified using the energy-throughput model. This model assumes that the degradation cost is directly proportional to the total energy processed by the battery, regardless of the operational patterns such as depth of discharge (DoD) and cycle average. Together with several other mainstream models, battery degradation will be discussed in section 2.3.

2.3. Battery Degradation

The increasing market share and relatively high performance of lithium-ion batteries have established them as a crucial component in EVs and various other applications, including energy arbitrage [28], renewable energy integration [29], frequency regulation [30] [31], and peak shaving [32].

In these profit-driven scenarios, the profitability of these services hinges on a balance between service revenue and operational costs, which are primarily influenced by battery degradation costs. Therefore, a comprehensive understanding of the relationship between battery operation and the degradation process is essential. This necessity has led to extensive research into the battery degradation process, resulting in the development of four categories of lithium-ion battery modeling [33]:

- **Physics-Based Models:** Physics-based models are derived from fundamental principles of battery electrochemistry, thermodynamics, and transport phenomena, providing accurate insights into the internal battery dynamics and degradation processes. The governing equations in these models are typically coupled partial differential equations, and the complexity is further exacerbated by the multi-factorial nature of lithium-ion battery degradation, resulting in exceedingly high cognitive and computational demands in rigorous physics-based models for practical applications. [34]. Consequently, these models are generally not used by non-chemical researchers [35].
- **Equivalent Circuit Models:** Equivalent circuit models represent lithium-ion batteries through an arrangement of circuit elements, including a voltage source for the open-circuit voltage, resistors for internal resistance, and RC networks for transient behaviors [36]. Battery aging is modeled by incorporating variable components [37], with parameter values typically derived from experimental data. The mathematical simplicity of these models makes them suitable for real-time applications [38].
- **Machine Learning Models:** Machine learning models estimate battery degradation through various techniques. Key approaches include regression models such as support vector regression [39], time series models such as long short-term memory [40], and physics-informed neural networks [41]. These data-driven methods can handle complex, non-linear relationships between input test data and target outputs (e.g., capacity fade, resistance increase) without requiring explicit mathematical expressions. However, the significant dependency on data and the lack of interpretability pose challenges for broader applications.
- **Empirical and Semi-empirical Models:** Empirical models, which are entirely data-driven, aim to depict battery degradation behavior through curve-fitted mathematical equations. Although these models can accurately match experimental data, their applicability is constrained to specific conditions, with significant errors arising when extrapolated to different operating conditions. On top of the empirical model, semi-empirical models integrate theoretical electrochemical phenomena, such as solid electrolyte interphase (SEI) growth [42] and lithium plating [43], with experimental data. By incorporating these mechanisms, semi-empirical models can potentially extend their validity beyond the specific experimental conditions. Additionally, the simplicity of empirical and semi-empirical models allows them to be applied in various scenarios like system design and optimizations.

2.3.1. Semi-Empirical Cyclic Degradation Model

To assess battery degradation and estimate associated costs, this study utilizes the semi-empirical degradation model developed by Xu et al. [42]. This model integrates the theory of SEI film formation with experimental data. Degradation is attributed to multiple stress factors, including temperature, average state of charge (SoC), and DoD. The fundamental principles of this model are summarized in the following equations:

$$L = 1 - \alpha_{sei} \cdot \exp(-f_{sei}) - (1 - \alpha_{sei}) \cdot \exp(-f_d) \quad (2.1)$$

In Equation 2.1, L denotes the battery capacity fade, where $L = 0$ indicates a new battery. α_{sei} is a constant that represents the portion of the charge capacity irreversibly consumed during the SEI film formation. The battery capacity can be divided into two terms: the SEI portion α_{sei} and the remaining capacity that fades at a rate proportional to the battery life $(1 - \alpha_{sei})$. In these two terms, f_{sei} and f_d are linearized SEI formation rate and linearized battery degradation rate, respectively. Since the usage and temperature also contribute to the SEI formation, f_{sei} is assumed to be proportional to f_d as in Equation 2.2. Substituting it back to Equation 2.1 yields Equation 2.3:

$$f_{sei} = \beta_{sei} f_d \quad (2.2)$$

$$L = 1 - \alpha_{sei} \cdot \exp(-\beta_{sei} f_d) - (1 - \alpha_{sei}) \cdot \exp(-f_d) \quad (2.3)$$

In practical cycle aging tests, the battery undergoes repeated charging and discharging over a specified number of cycles, with its state of health (SoH) being recorded throughout the process. Given that test conditions, such as DoD, charging/discharging power, and temperature, are typically kept constant, Equation 2.3 can be reformulated to be applied to the cycling aging test data as follows:

$$L_{cyc} = 1 - \alpha_{sei} \cdot \exp(-\beta_{sei} N f_{d,1}) - (1 - \alpha_{sei}) \cdot \exp(-N f_{d,1}) \quad (2.4)$$

In Equation 2.4, N denotes the number of cycles that the battery undergoes and $f_{d,1}$ is the linearized degradation rate per cycle. A fitting algorithm can then be used to determine the value of α_{sei} , β_{sei} , and $f_{d,1}$ as in Figure 2.1. As observed, a new lithium-ion battery experiences rapid degradation during the first few hundred cycles. Subsequently, the degradation rate slows once the battery life decreases to approximately 0.9, indicating the completion of SEI formation.

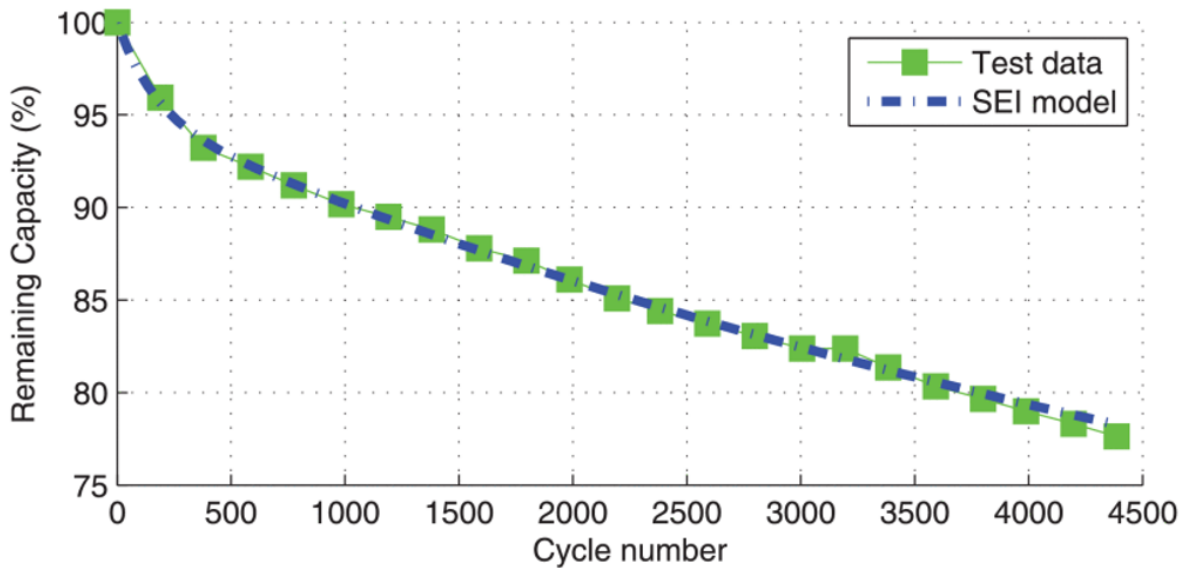


Figure 2.1: An example of degradation curve and the fitting of the SEI model from [42]

2.3.2. Stress Factor Models

In practice, battery degradation is significantly influenced by operational patterns and ambient conditions. Therefore, the linearized degradation rates discussed in subsection 2.3.1 are modeled as functions of several factors, including depth of discharge (DoD), state of charge (SoC), cell temperature, and elapsed time, among others. Assuming that these factors are independent, the linearized cyclic degradation rate can be expressed as:

$$f_c(\delta, \sigma, T_c) = S_\delta(\delta)S_\sigma(\sigma)S_T(T_c) \quad (2.5)$$

In Equation 2.5, $S_\delta(\delta)$, $S_\sigma(\sigma)$ and $S_T(T_c)$ denote the stress factors of DoD, Soc and cell temperature, respectively. By replacing $S_\delta(\delta)$ with the time stress factor $S_t(t)$, the calendar degradation rate can be expressed by:

$$f_t(t, \sigma, T_c) = S_t(t)S_\sigma(\sigma)S_T(T_c) \quad (2.6)$$

In this study, the linearized degradation rate per cycle is calculated using Equation Equation 2.7. The focus is solely on the impact of Depth of Discharge (DoD), leading to a simplified expression for the linearized degradation rate, as shown in [44].

$$f_{d,1} = [S_\delta(\delta) + S_t(t)]S_\sigma(\sigma)S_T(T_c) \quad (2.7)$$

According to the literature, the DoD stress factor can be categorized into two types: exponential models [44] and quadratic models [45]. In this study, two different types of battery chemistries are compared: lithium ferrophosphate (LFP) and lithium manganese oxide (LMO). For LFP battery this study adopts the exponential stress factor model, as in Equation 2.8. And for LMO battery, one more coefficient is introduced as in Equation 2.9.

$$f_{d,1,LFP} = S_\delta(\delta) = k_{\delta,1} \cdot \delta e^{k_{\delta,2}\delta} \quad (2.8)$$

$$f_{d,1,LMO} = S_\delta(\delta) = (k_{\delta,1} \cdot \delta^{k_{\delta,2}} + k_{\delta,3})^{-1} \quad (2.9)$$

It is important to note that all calculations of battery degradation are based on full cycles; however, in practice, the battery does not always operate at full cycle. This requires the conversion of irregular cycles to equivalent full cycles. In this study, Miner's rule [46] is applied for this conversion, as shown in Equation 2.10:

$$N_{eq,i} = \frac{N_{life[\delta=1]}}{N_{life[\delta=\delta_i]}} \quad (2.10)$$

Where $N_{eq,i}$ is the equivalent 100% DoD cycle number of the i th counted cycle; $N_{life[\delta=1]}$ and $N_{life[\delta=\delta_i]}$ refer to the battery lifetime number of cycles under 100% and δ_i DoD. The battery capacity fade under irregular cycles can there for be expressed as in Equation 2.11:

$$L_{cyc} = 1 - \alpha_{sei} \cdot \exp(-\beta_{sei} \cdot f_{d,1[\delta=1]} \sum_{i=1}^n N_{eq,i}) - (1 - \alpha_{sei}) \cdot \exp(-f_{d,1[\delta=1]} \sum_{i=1}^n N_{eq,i}) \quad (2.11)$$

The state of health (SoH) versus cycle number curves for the LFP and LMO batteries under different DoD are shown in Figure 2.2. After converting the irregular cycles to equivalent full cycles using Miner's rule, the SoH versus equivalent full cycles is presented in Figure 2.3. As observed, when operating under full cycles, the LMO battery exhibits a faster degradation rate and, consequently, a shorter cycle life compared to the LFP battery.

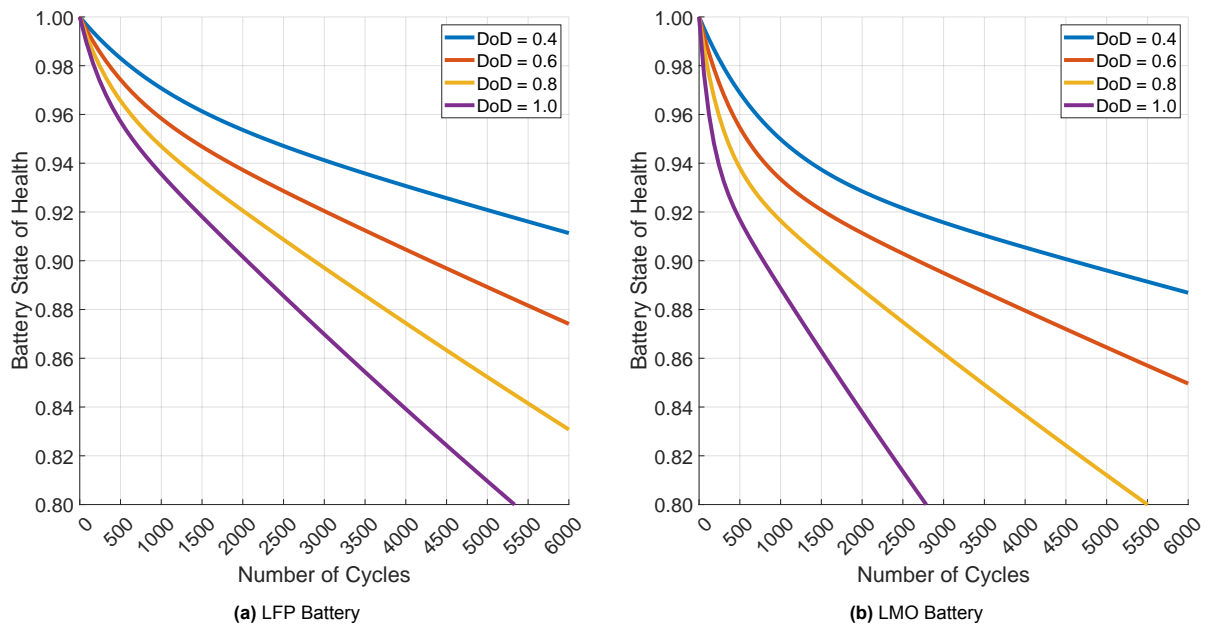


Figure 2.2: Battery state of health versus cycle number under different depth of discharge

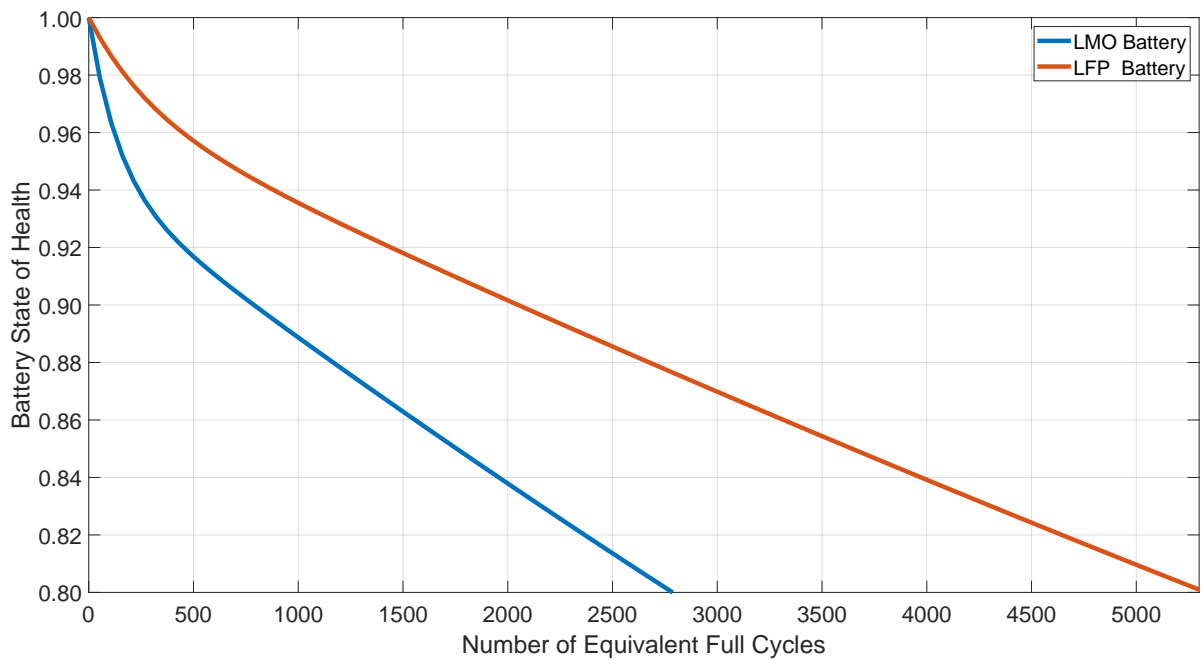


Figure 2.3: Battery state-of-health versus number of equivalent full cycles of LFP and LMO battery

2.3.3. Semi-Empirical Calendar Aging Model

In the previous subsections, we introduced the semi-empirical cyclic degradation model and the stress factor model, which enable the estimation of battery cyclic degradation. However, in practical applications, another significant contributor to battery capacity loss is calendar aging. Calendar aging occurs even when the cell remains in idle state and arises from side reactions caused by the thermodynamic instability of the materials [47].

In various lithium-ion battery applications, such as frequency containment reserve (FCR), electric vehicles (EVs), and energy arbitrage, as will be discussed in this study, the operational period is often significantly shorter than the idle period [48], [49]. This necessitates an investigation into the effects of calendar aging. Studies such as [49], [50] and [51] have formulated the calendar aging process of lithium ferrophosphate (LFP) batteries using semi-empirical models, with parameters that can be curve-fitted based on accelerated laboratory calendar test data.

Typically, calendar aging can be categorized into two types: reversible and irreversible capacity loss [33]. In this study, all capacity losses due to calendar aging are considered irreversible. Similar to the stress factor model used in cyclic degradation estimation, the calendar aging rate can also be attributed to several stress factors, such as storage temperature and state of charge (SoC). The semi-empirical model presented in [52] is utilized to estimate the battery calendar life behaviour in this study, and the two types of lithium ion batteries are assumed to share the same calendar degradation model. The primary concept of this model can be summarized by Equation 2.12:

$$L_{cal} = \alpha_{cal,1} \cdot \exp(\alpha_{cal,2} \cdot SoC_{sto}) \cdot \exp((\alpha_{cal,3} \cdot SoC_{sto} + \alpha_{cal,4})/T_{sto}) \cdot t^p \quad (2.12)$$

According to the calendar aging equation, the lithium-ion battery calendar degradation curves under different storage SoC and temperature are depicted in Figure 2.4.

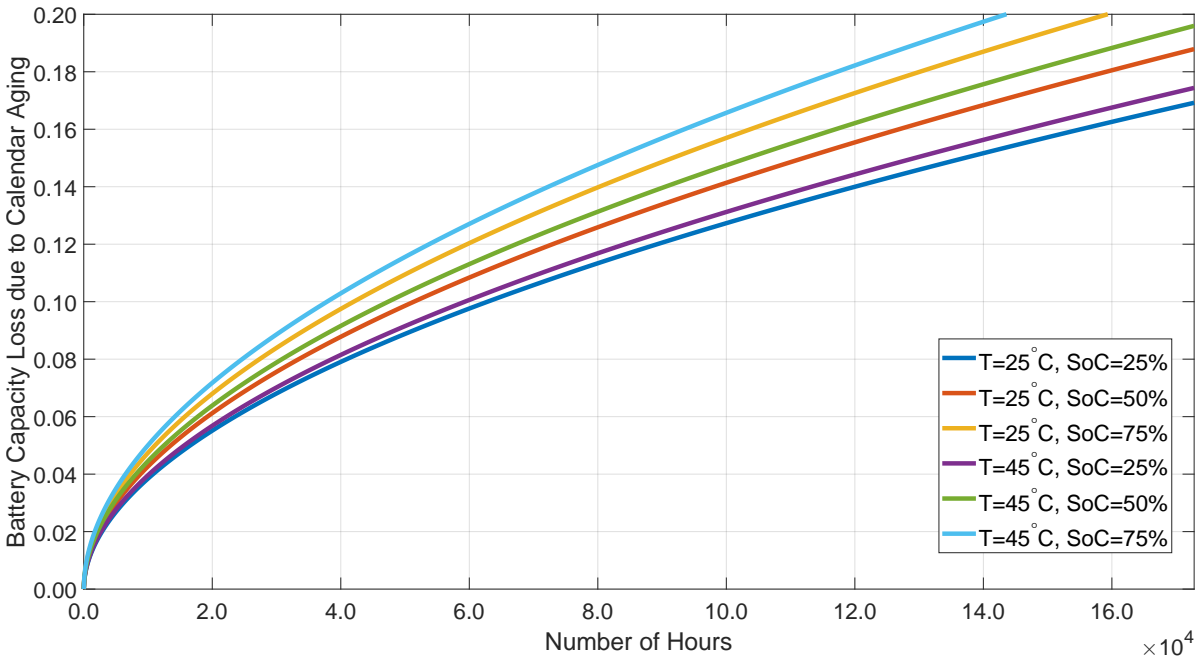


Figure 2.4: The battery capacity loss due to calendar aging versus number of hours at different temperature and SoC

3

Problem Formulation

3.1. System Composition

The spatial temporal arbitrage system consists of the following components: a fully electric truck and three Alfen *TheBattery Mobile X* modules. As Alfen's 4th generation mobile battery energy storage system (BESS), it reliably supplies the necessary power and energy for applications such as events, construction sites, and EV charging hubs. Each module offers an energy capacity of up to 720 kWh and a power capacity of 270 kW [53].

The proposed portable energy storage system (PESS) utilizes a 800-km E-mobility to travel between different zones as shown in Figure 3.1, with an energy consumption rate of approximately 1.25 kWh per kilometer. This configuration gives an energy capacity of about 1 MWh, with 840 kWh allocated for arbitrage and the remaining capacity dedicated to transportation. Key technical and cost specifications of the system are given in Table 3.1.

Table 3.1: Technical specification and cost estimation of the proposed spatial temporal arbitrage model

Parameter	Unit	Value	Parameter	Unit	Value
Battery Price LFP	€/kWh	140	System Power	kW	1,125
Battery Price LMO	€/kWh	110	Mobile X Capacity	kWh	2,160
Connection Price	€/MW	34,000	E-mobility Capacity	kWh	840
E-mobility Price	€	62,400	System Capacity	kWh	3,000
Inverter Price	€	75,600			

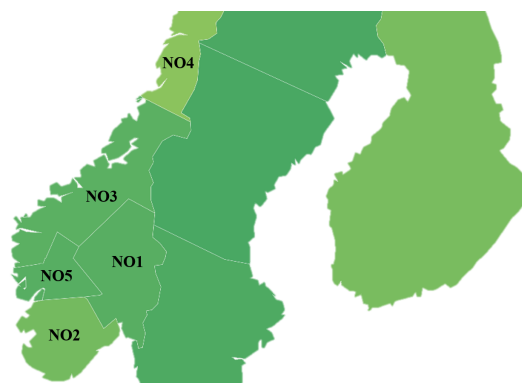


Figure 3.1: Different bidding zones in Norway

3.2. Model Input: Norwegian Zonal Day-ahead Market Price

The economic feasibility of the proposed PESS is evaluated in the Norwegian day-ahead market (DAM). Norway is divided into five distinct bidding zones as illustrated in Figure 3.1. Due to its relative isolation and similar electricity tariff to NO3 (as shown in Figure 3.2), bidding zone NO4 is excluded from the scope of this study. Additionally, since the bidding prices of zones NO1 and NO5 are observed to be nearly identical for most of the year (Figure 3.3), these two zones are treated as one with uniform price in this study.

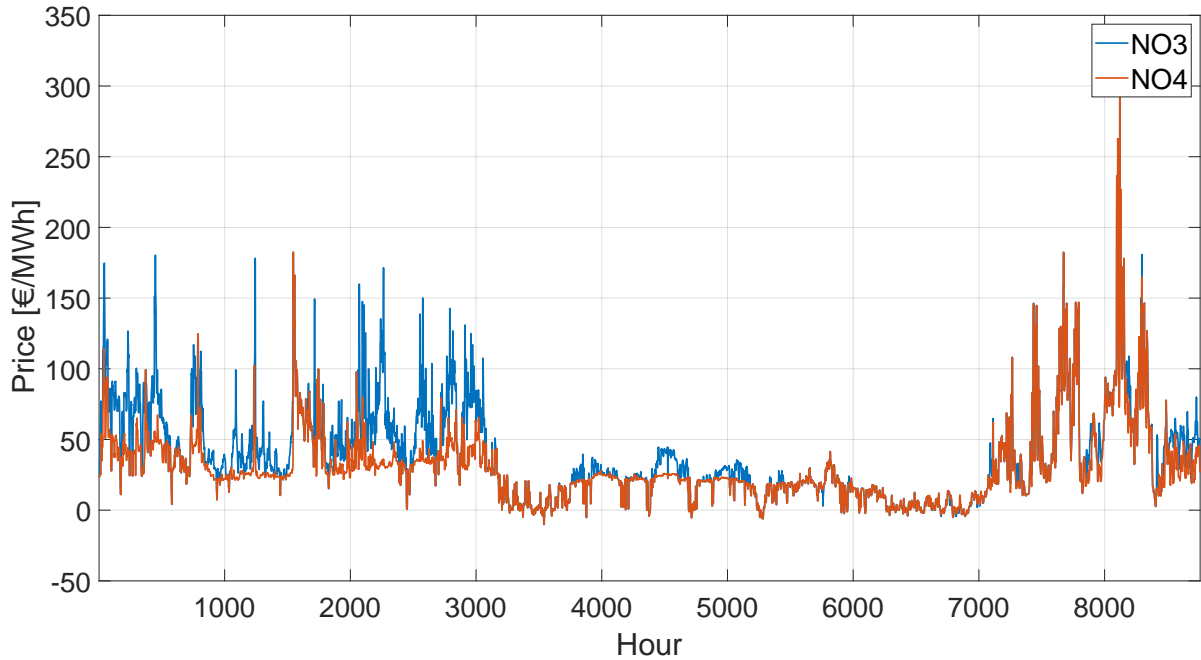


Figure 3.2: Comparison of day ahead market hourly prices between NO3 and NO4 in 2023 [54]

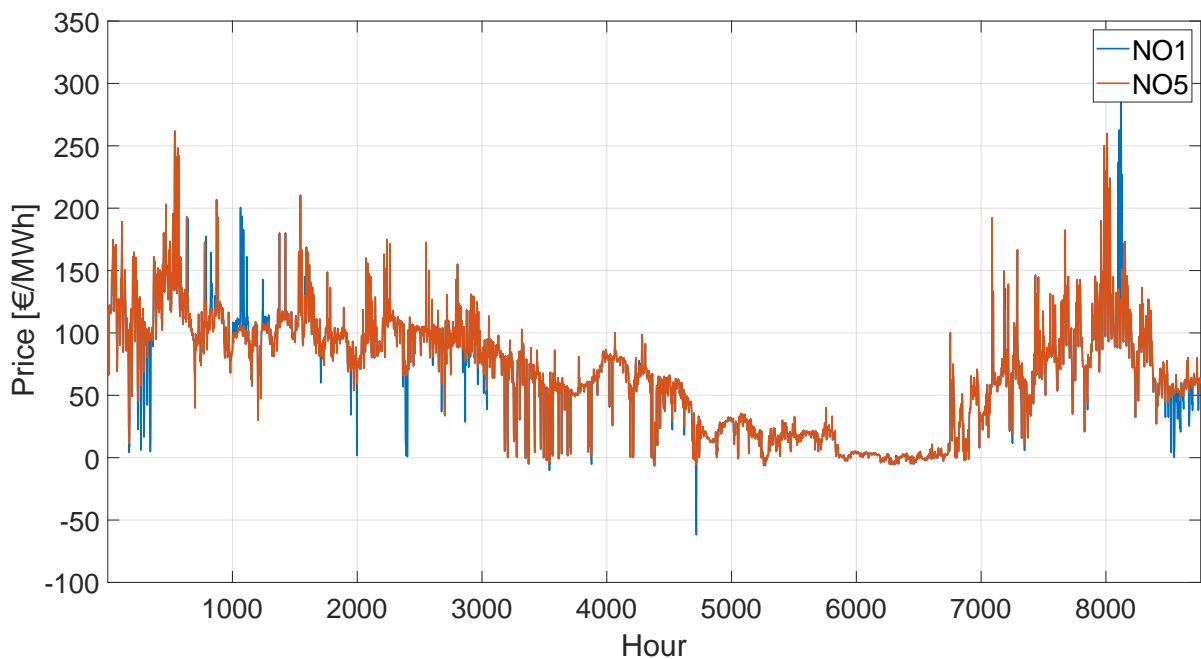


Figure 3.3: Comparison of day ahead market hourly prices between NO1 and NO5 in 2023 [54]

The complete hourly tariff for the year 2023 across all bidding zones are given in Figure 3.4.

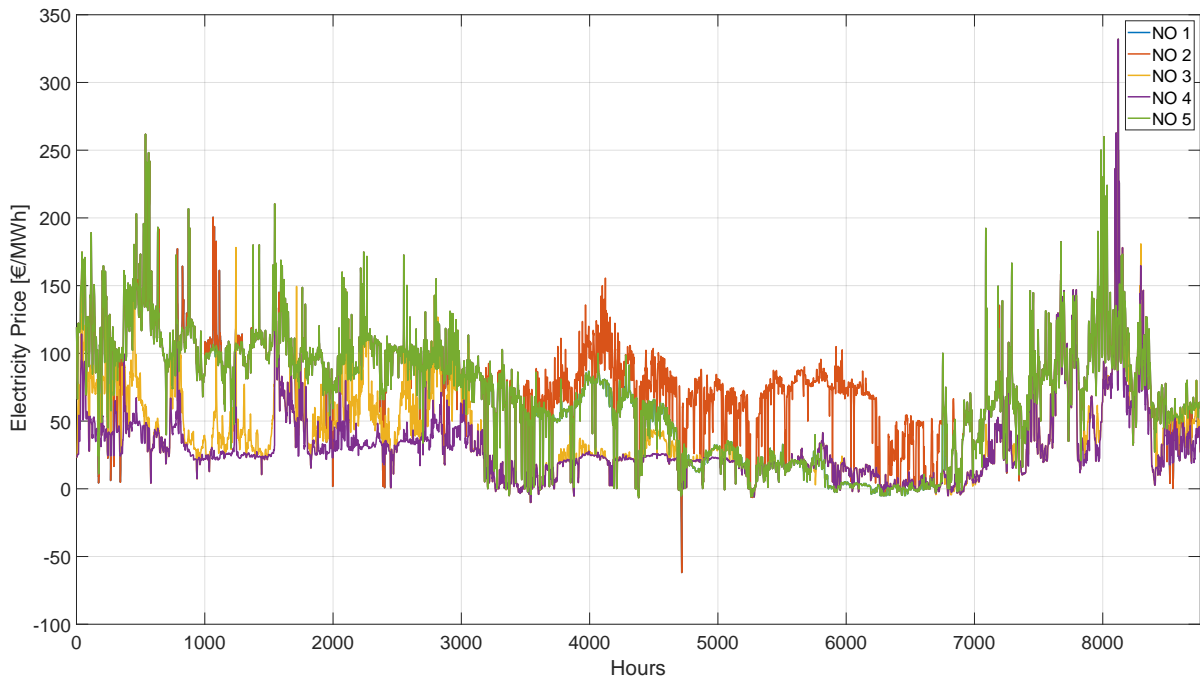


Figure 3.4: Day ahead market hourly prices of all 5 Norwegian bidding zones

Since the travel and charging/discharging scheduling of the proposed system is carried out on a daily basis, the system input would be the hourly DAM electricity in different bidding zones as in Figure 3.5.

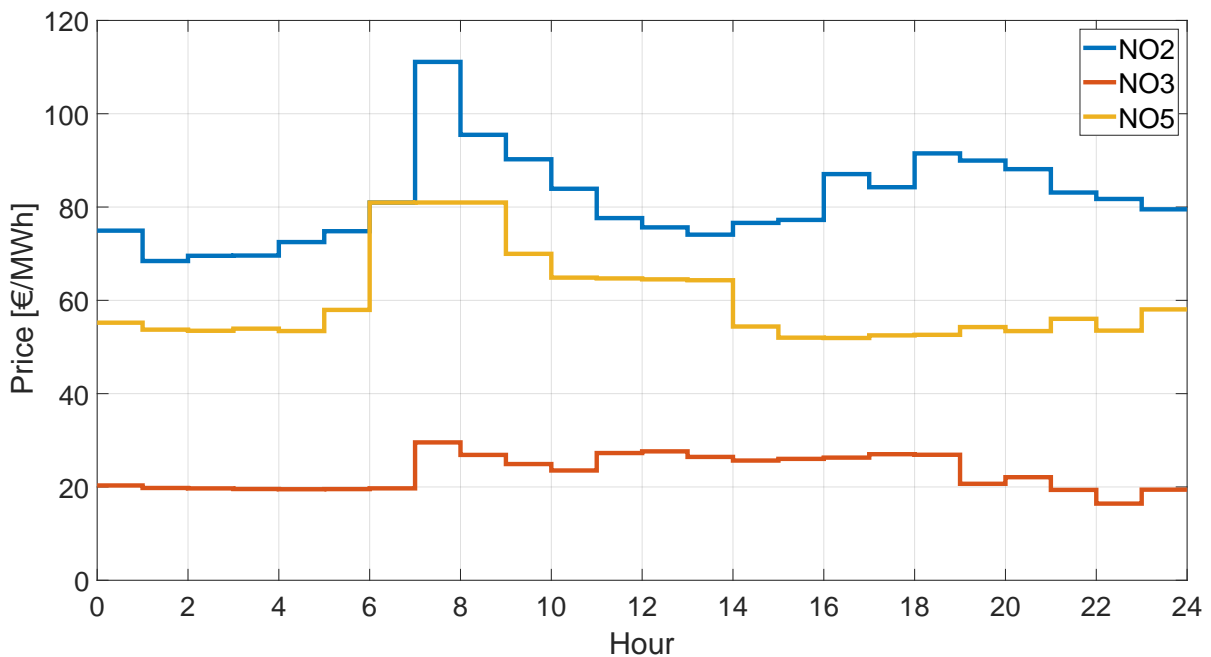


Figure 3.5: An example of hourly day-ahead electricity tariffs in different Norwegian bidding zones on day 158 [54]

3.3. Objective Function

The operational schedule optimization of the proposed system is formulated as a mixed integer linear programming (MILP) problem in this study. The optimal daily schedule is derived by maximizing the daily profit, which is composed of three key components: arbitrage revenue R , transportation cost C^T and degradation cost C^D as in Equation 3.1.

$$\begin{aligned} obj(x_t) &= R(x_t) - C^T(x_t) - C^D(x_t) \\ \text{where } x_t &= [P_n^{dis}(t), P_n^{chg}(t), \gamma_{nm}(t), \omega_n(t), \alpha_n(t), \beta_n(t), \theta_n(t) \quad \forall n, m \in \Omega, t \in H] \end{aligned} \quad (3.1)$$

In the equation, Ω and H represent the bidding zone location domain and optimization horizon. The decision variable x_t includes the scheduling of the following elements: $P_n^{Dis}(t)$ and $P_n^{Chg}(t)$, which represent the discharging/charging power in bidding zone n during time slot t , respectively. Additionally, binary variable $\gamma_{nm}(t)$ denotes travel from bidding zone n to m at time slot t ; $\alpha_n(t)$ and $\beta_n(t)$ indicate arrival at and departure from bidding zone n at time slot t ; and $\theta_n(t)$ serves as an auxiliary binary variable to keep the variable $\alpha_n(t)$ consistent with the arrival.

3.3.1. Objective Function: Arbitrage Revenue

The arbitrage revenue can be expressed as in Equation 3.2. In the equation, Δt is the simulation time step, which is set to 60 minutes and $\lambda_n(t)$ is the electricity tariff in bidding zone n at time slot t .

$$R(x_t) = \Delta t \sum_{t \in H} \sum_{n \in \Omega} \lambda_n(t) [P_n^{dis}(t) - P_n^{chg}(t)] \quad (3.2)$$

3.3.2. Objective Function: Transportation Cost

The primary component of operational costs is transportation, which includes driver wages and fuel expenses. As referenced in [55], the hourly wage for a heavy truck driver in Norway is approximately €20 per hour. The fuel cost per hour is estimated based on an assumed truck speed of 50 km/h and an hourly energy consumption of approximately 62.5 kWh. Since the PESS primarily charges during low-price hours, the electricity tariff is assumed to be below €30 per MWh, resulting in a marginal fuel cost of €1.8 per hour. Consequently, the hourly transportation cost c^T is set at €22. The daily system transportation cost can be calculated using Equation 3.3.

$$C^T(x_t) = c^T \Delta t \sum_{t \in H} \sum_{n \in \Omega} \sum_{m \in \Omega} \gamma_{nm}(t) \quad (3.3)$$

3.3.3. Objective Function: Cyclic Degradation Cost

This thesis presents a comparative analysis of two distinct formulations for degradation cost. The first formulation is based on energy throughput degradation model, and the second utilizes a semi-empirical degradation model.

- **Energy Throughput Model Formulation**

The energy throughput model formulation is presented in Equation 3.4, where c^D represents a constant quantifying the degradation cost per MWh. In this model, battery degradation is independent of the current state of health (SoH) and operational patterns, meaning that the degradation cost is solely determined by the amount of energy processed by the battery.

$$C^D = c^D \Delta t \sum_{t \in H} \sum_{n \in \Omega} [P_n^{dis}(t) + P_n^{chg}(t)] \quad (3.4)$$

- **Semi-Empirical Model Formulation**

As the semi-empirical model employed in this study is cycle-based, it requires a cycle counting algorithm to extract relevant information for each cycle. An online cycle counting algorithm is utilized to determine cycle characteristics, such as depth of discharge (DoD), from the daily energy

profile. A more detailed explanation of the online cycle counting algorithm is given in subsection 3.4.3.

To formulate the degradation cost using the semi-empirical model, the non-linear relationship between the DoD and battery life needs to be examined first. As discussed in subsection 2.3.1, battery degradation follows a double exponential relationship with the cycle number N and degradation rate $f_{d,1}$, which is dependent on the DoD. Equation 3.5 is presented again for reference.

$$L_{cyc} = 1 - \alpha_{sei} \cdot \exp(-\beta_{sei} \cdot NS_{\delta}(\delta)) - (1 - \alpha_{sei}) \cdot \exp(-NS_{\delta}(\delta)) \quad (3.5)$$

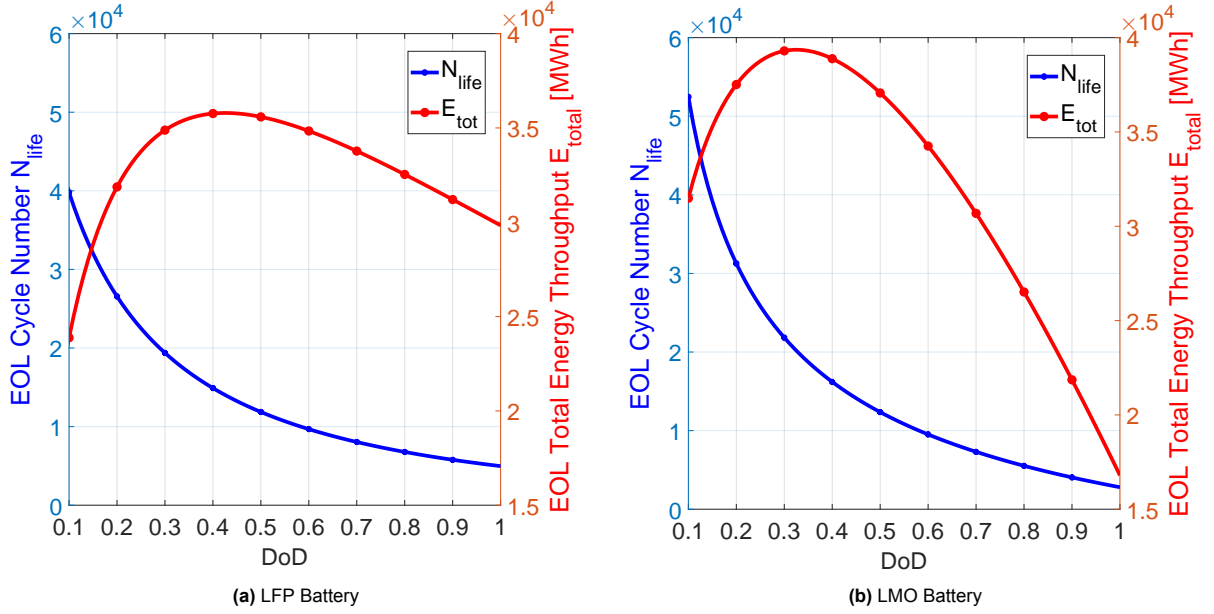


Figure 3.6: Two different types of battery life time cycle number and energy throughput versus DoD

By setting the left-hand side of Equation 3.5 to the end-of-life degradation L_{eol} , which is normally valued at 0.2, the end-of-life cycle number N_{eol} and lifetime energy throughput E_{total} at certain DoD can be determined. The relationship between these two lifetime values and the DoD for two different battery chemistries are illustrated in Figure 3.6.

Given the battery replacement cost C^{rep} , the degradation cost per unit energy $c^D(DoD)$ at a specific DoD can be calculated using Equation 3.6. The degradation cost for each cycle with a certain depth, $C^{cyc}(DoD)$, can then be determined by multiplying the cost per unit energy by the amount of energy, as expressed in Equation 3.7.

$$c_{unit}^{cyc}(DoD) = \frac{C^{rep}}{E_{eol}(DoD)} \quad (3.6)$$

$$C^{cyc}(DoD) = E^{PESS} \cdot \sum_{t \in H} c_{unit}^{cyc}(DoD) \cdot DoD(t) \quad (3.7)$$

The relationship between degradation cost per MWh and cost per cycle as a function of DoD is illustrated in Figure 3.7a and Figure 3.8a. It can be observed that the optimal cycle depth lies between 0.3 and 0.6 for LFP and between 0.2 and 0.5 for LMO, corresponding to the highest lifetime energy throughput shown in Figure 3.6. To incorporate the non-linear semi-empirical degradation cost model into the mixed-integer linear programming (MILP) framework, a piecewise linear approximation is utilized, as depicted in Figure 3.7b and Figure 3.8b.

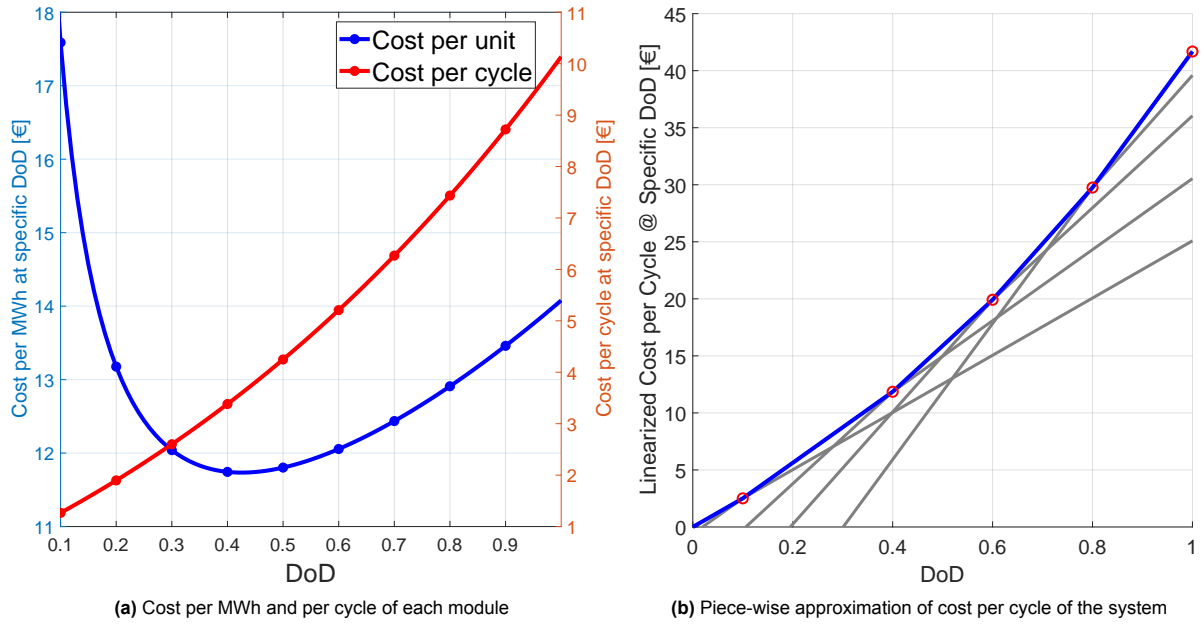


Figure 3.7: LFP battery cyclic cost per MWh and cost per cycle

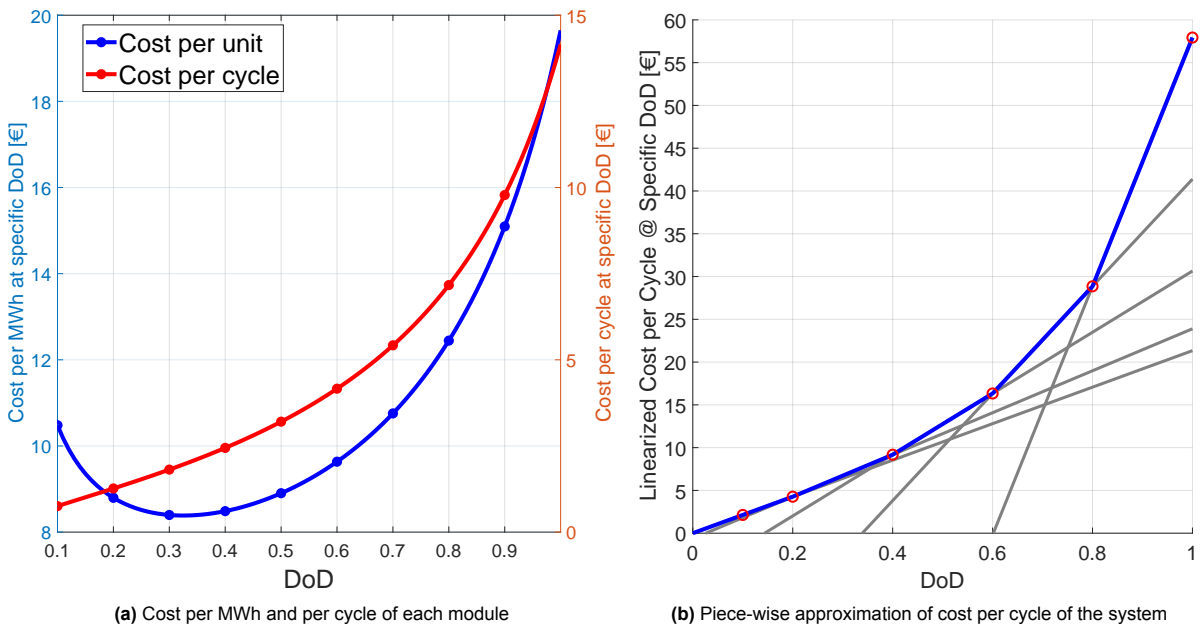


Figure 3.8: LMO battery cyclic cost per MWh and cost per cycle

In the preceding sections, the impact of the operational pattern, specifically DoD, on the degradation rate has been discussed. This discussion has so far assumed that the impact is independent of the current battery state-of-health (SoH). However, as shown in Figure 2.3, identical cycles will cause varying degrees of damage to the battery depending on its SoH. To formulate the degradation cost using the complete semi-empirical model, the effect of SoH needs to be accounted for and is represented as a scaling factor S_{SoH} as in Equation 3.8.

$$S^{SoH}(N) = \frac{\partial L}{\partial N} \cdot \frac{C^{rep}}{L_{eol} \cdot C_{DoD=100\%}^D} \quad (3.8)$$

The relationship between the scaling factor S^{SoH} and the accumulated full cycles N_{total} is illustrated in Figure 3.9. Notably, an upper bound of S_{max}^{SoH} is incorporated into the model, corresponding to a maximum full-cycle degradation cost around €70. This adjustment is needed because, without the upper limit, the degradation cost term in the objective function would be excessively high during the initial few hundred cycles, which would discourage the battery from engaging in any charging or discharging actions. The final formation of degradation cost is given in Equation 3.9.

$$C_{deg}^{cyc} = C^{cyc}(DoD) \cdot S^{SoH} \quad (3.9)$$

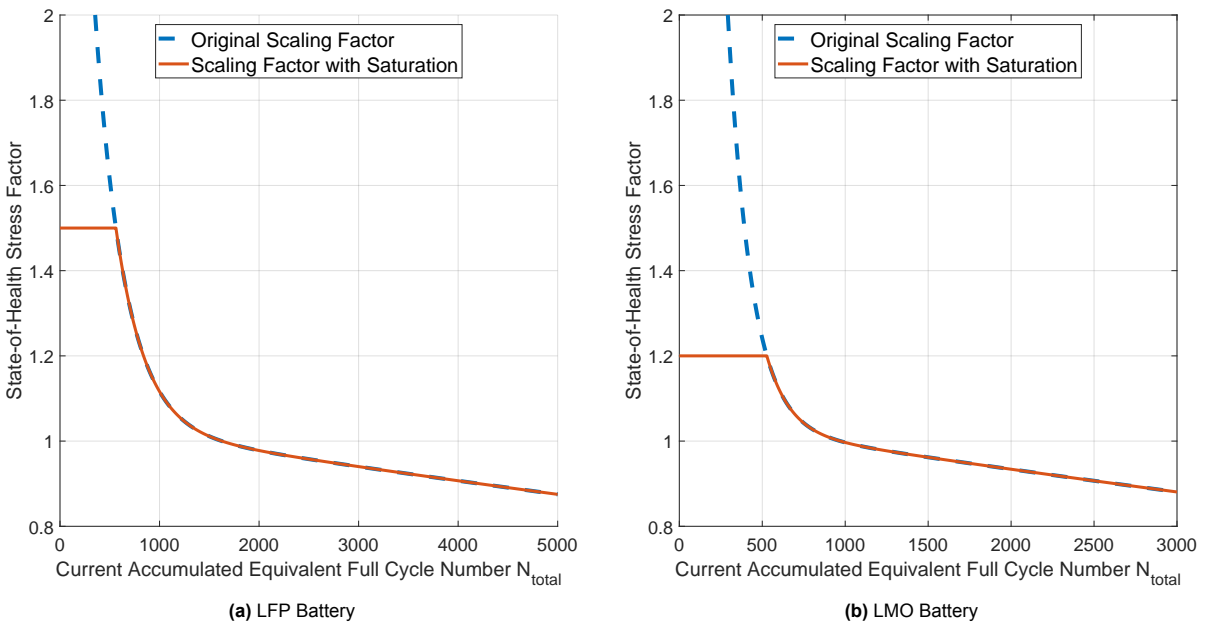


Figure 3.9: State-of-Health stress factor versus accumulated equivalent full cycle N_{total}

3.3.4. Objective Function: Calendar Degradation Cost

The calendar degradation cost term is formulated based on the semi-empirical calendar degradation model proposed in [52]. Similar to cyclic degradation term formulation, the calendar cost term is calculated based on Equation 2.12, which is given here again for reference.

$$L_{cal} = \alpha_{cal,1} \cdot \exp(\alpha_{cal,2} \cdot SoC_{sto}) \cdot \exp((\alpha_{cal,3} \cdot SoC_{sto} + \alpha_{cal,4})/T_{sto}) \cdot t^p \quad (3.10)$$

In this study, the battery module storage temperature is considered to be fixed at $T_{sto} = 25^\circ C$. Consequently, varying storage state-of-charge (SoC) will result in different calendar life time $t_{eol}(SoC)$ for a given end-of-life degradation $L_{cal}^{eol} = 0.2$, and the corresponding calendar cost per hour $c_{hour}^{cal}(SoC)$ can be determined by Equation 3.11. The daily calendar degradation cost is calculated based on the daily average SoC as in Equation 3.12.

$$c_{hour}^{cal}(SoC) = \frac{C^{rep}}{t_{eol}(SoC)} \quad (3.11)$$

$$C_{deg}^{cal}(SoC) = 24 \cdot c_{hour}^{cal} \left[\sum_{t \in H} SoC(t)/24 \right] \quad (3.12)$$

The battery calendar life and daily calendar cost of LFP and LMO battery are depicted in Figure 3.10.

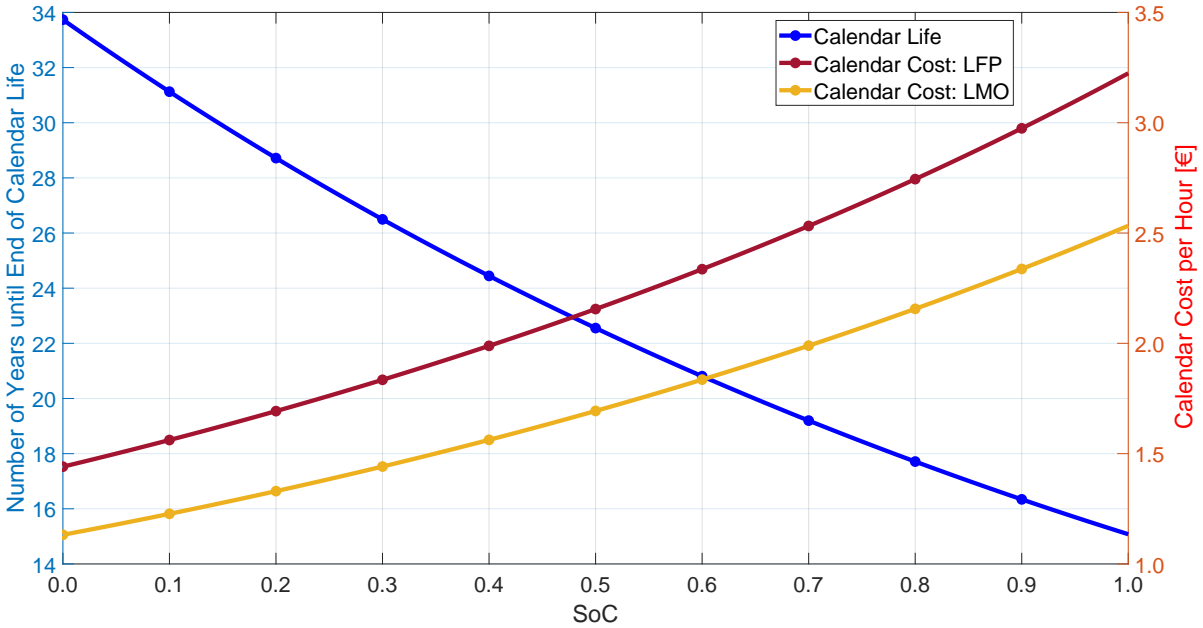


Figure 3.10: Battery calendar life time and storage cost per hour versus SoC

3.4. Constraints

For a complete formulation of the MILP model, constraints are needed in addition to the objective function to define the feasible regions and solution space. In this study, constraints can be divided into three categories: 1. battery operation constraints; 2. transportation constraints and 3. cycle counting constraints.

3.4.1. Constraints: Battery Operation

The system is considered to have an energy conversion efficiency of η , the self discharge rate is assumed to be 0 in this study. The energy balance and energy level constraints can be expressed in Equation 3.13 and Equation 3.14. And the state of charge level at time t can be calculated as in Equation 3.15.

$$E(t) = E(t-1) + \Delta t \sum_{n \in \Omega} [P_n^{chg}(t)\eta - P_n^{dis}(t)/\eta] \quad \forall t \in H \quad (3.13)$$

$$0 \leq E(t) \leq SoH \cdot E^{max} \quad \forall t \in H \quad (3.14)$$

$$SoC(t) = \frac{E(t)}{SoH \cdot E^{max}} \quad \forall t \in H \quad (3.15)$$

Charging/discharging power constrains in Equation 3.16 and Equation 3.17 indicate that the battery must be parked at a specific node and be in corresponding operation mode in order to charge/discharge. Operation status constraint in Equation 3.18 ensures that the battery does not charge and discharge at the same time:

$$0 \leq P_n^{chg}(t) \leq \omega_n(t) Z^{chg}(t) P^{max} \quad \forall n \in \Omega, t \in H \quad (3.16)$$

$$0 \leq P_n^{dis}(t) \leq \omega_n(t) Z^{dis}(t) P^{max} \quad \forall n \in \Omega, t \in H \quad (3.17)$$

$$Z^{chg}(t) + Z^{dis}(t) \leq 1 \quad \forall t \in H \quad (3.18)$$

3.4.2. Constraints: Transportation

The transportation constraints follows the PESS model in [23], and it comprises the following equations: Equation 3.19 ensures that the battery can only be either parked in one location or traveling from one location to another at every time step. Equation 3.20 links the binary arrival and departure indicator $\alpha_n(t)$, $\beta_n(t)$ with the location indicator $\omega_n(t)$ and Equation 3.21 makes sure the arrival and departure at the same location do not occur simultaneously.

$$\sum_{n \in \Omega} \omega_n(t) + \sum_{n \in \Omega} \sum_{m \in \Omega} \gamma_{nm}(t) \leq 1 \quad \forall n, m \in \Omega, t \in H \quad (3.19)$$

$$\alpha_n(t) - \beta_n(t) = \omega_n(t) - \omega_n(t-1) \quad \forall n \in \Omega, t \in H \quad (3.20)$$

$$\sum_{n \in \Omega} \alpha_n(t) \leq 1 - \sum_{n \in \Omega} \beta_n(t) \quad \forall t \in H \quad (3.21)$$

Equation 3.22 will set the binary travel indicator $\gamma_{nm}(t)$ to 1 when a departure occurs and Equation 3.23 ensures that this travel indicator corresponds to the travel between the departure and arrival locations. The value of the auxiliary binary variable $\theta_m(t)$ that appeared in Equation 3.23 is linked to the arrival indicator by Equation 3.24 so that the value of $\alpha_m(t)$ can be reset at the end of every transportation. Equation 3.25 specifies the time for travel and loading/unloading the battery between every node.

$$\sum_{m \in \Omega} \gamma_{nm}(t) \geq \beta_n(t) \quad \forall n \in \Omega, t \in H \quad (3.22)$$

$$\alpha_m(t) - \theta_m(t) = \sum_{n \in \Omega} [\gamma_{nm}(t-1) - \gamma_{nm}(t)] \quad \forall m \in \Omega, t \in H \quad (3.23)$$

$$\sum_{n \in \Omega} \alpha_n(t) \leq 1 - \sum_{n \in \Omega} \theta_n(t) \quad \forall t \in H \quad (3.24)$$

$$\gamma_{nm}(t) \geq \gamma_{nm}(t-1) - \gamma_{nm}(t-d_{nm}) \quad \forall n, m \in \Omega, t \in H \quad (3.25)$$

A daily power profile of the relocatable energy storage system is given in Figure 3.11, serving as an example to explain the operation of transportation constraints. Between hours 10 and 19, the system undergoes two relocations: initially from NO3 to NO1 at $t = 13$, followed by a return from NO1 to NO3 at $t = 17$. The corresponding values of the transportation constraint binary variables during this period are presented in Table 3.2.

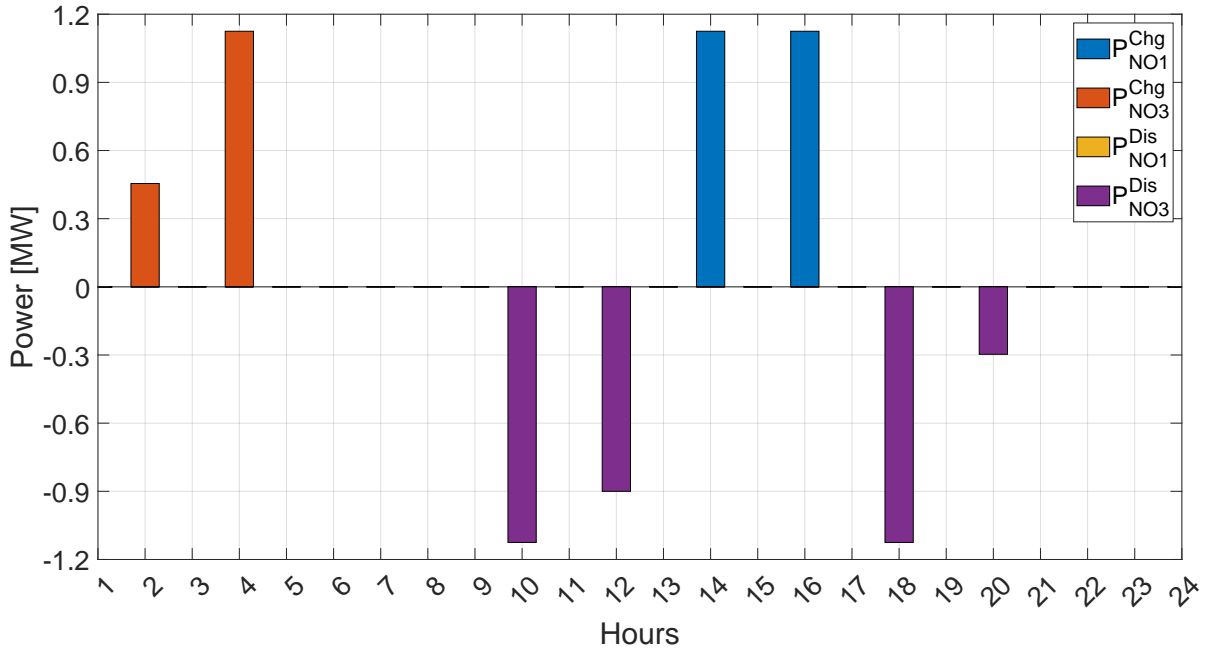


Figure 3.11: A daily power profile example to illustrate the working principle of transportation constraints

Table 3.2: Values of binary transportation variables between hour 10 and 19 in Figure 3.11

t	10	11	12	13	14	15	16	17	18	19
$\omega_1(t)$	0	0	0	0	1	1	1	0	0	0
$\omega_3(t)$	1	1	1	0	0	0	0	0	1	1
$\alpha_1(t)$	0	0	0	0	1	0	0	0	0	0
$\alpha_3(t)$	0	0	0	0	0	0	0	0	1	0
$\beta_1(t)$	0	0	0	0	0	0	0	1	0	0
$\beta_3(t)$	0	0	0	1	0	0	0	0	0	0
$\gamma_{13}(t)$	0	0	0	0	0	0	0	1	0	0
$\gamma_{31}(t)$	0	0	0	1	0	0	0	0	0	0
$\theta_1(t)$	0	0	0	1	0	0	0	0	0	0
$\theta_3(t)$	0	0	0	0	0	0	0	1	0	0

3.4.3. Constraints: Real-time Cycle Counting Algorithm

As discussed in [42], the cycle-based semi-empirical model is employed together with the rainflow counting algorithm (RCA). However, RCA necessitates the availability of the complete SoC profile to derive the counting result; whereas in a mixed-integer linear programming (MILP) problem, the SoC profile is unknown during the optimization process. Furthermore, the rainflow algorithm does not have a closed-form, which poses challenges for its application in MILP formulation [56].

Shi et al. [57] integrated RCA into battery operation optimization by utilizing a subgradient algorithm to minimize the non-differentiable degradation cost term. They transformed the constrained objective function into an unconstrained form via a log-barrier function [58]. By appropriately adjusting the step length in each iteration, the desired accuracy in the final result can be guaranteed.

However, the subgradient method is not applicable in those mainstream optimizer like Gurobi and Cplex. Additionally, it requires a more complicated objective function formulation, a user-defined update rule in each iteration for charging and discharging power that involves the partial derivative calculation. For simplicity, this thesis will use a real-time cycle counting method proposed in [59]. The main idea of this algorithm can be concluded by the following equations.

$$Z^{chg}(t) - Z^{chg}(t-1) = Z_{st}^{chg}(t) - Z_{end}^{chg}(t) \quad \forall t \in H \quad (3.26)$$

$$Z^{dis}(t) - Z^{dis}(t-1) = Z_{st}^{dis}(t) - Z_{end}^{dis}(t) \quad \forall t \in H \quad (3.27)$$

$$Z^{CC}(t) = Z_{end}^{chg}(t) + Z_{end}^{dis}(t) \quad \forall t \in H \quad (3.28)$$

Equation 3.26 and Equation 3.27 establish the relationship between the charging/discharging start and end indicators and the variation of the charging/discharging states. Equation 3.28 ensures that the end-of-cycle indicator $Z^{CC}(t)$ is set to 1 whenever a charging or discharging cycle ends.

Equation 3.29 describes how the auxiliary SoC variable is determined based on the end-of-cycle indicator $Z^{CC}(t)$: when a cycle ends, the auxiliary SoC variable $x(t)$ gets the SoC value from the previous time step. Otherwise, it continues to inherit the value of $x(t-1)$ from the previous moment.

$$x(t) = \begin{cases} x(t-1) & \text{if } Z^{CC}(t) = 0 \\ SoC(t-1) & \text{if } Z^{CC}(t) = 1 \end{cases} \quad \forall t \in H \quad (3.29)$$

$$DoD(t) = |SoC(t-1) - x(t-1)| \quad \forall t \in H \quad (3.30)$$

Since the if-else condition in Equation 3.29 and the absolute value in Equation 3.30 are not linear, these two equations need to be linearized to be applied in the MILP model. Equation 3.29 can be linearized by the big-M method as in Equation 3.31. And the absolute value can be expressed as in Equation 3.32.

$$-M \cdot Z^{CC}(t) \leq x(t) - x(t-1) \leq M \cdot Z^{CC}(t) \quad \forall t \in H \quad (3.31a)$$

$$-M \cdot [1 - Z^{CC}(t)] \leq x(t) - SoC(t-1) \leq M \cdot [1 - Z^{CC}(t)] \quad \forall t \in H \quad (3.31b)$$

$$DoD(t) \geq SoC(t-1) - x(t-1) \quad \forall t \in H \quad (3.32a)$$

$$DoD(t) \geq -SoC(t-1) + x(t-1) \quad \forall t \in H \quad (3.32b)$$

For more details about the functionality of online cycle counting algorithm, an example SoC profile is presented in Figure 3.12, with its corresponding continuous and binary variable values listed in Table 3.3. The online counting algorithm counts a half-cycle one unit time step after its completion, resulting in a 'delay' between the actual and counted cycle ends. For instance, Figure 3.12 illustrates three half-cycles of magnitudes 0.3, 0.5, and 0.2 occurring at $t = 2$, $t = 7$, and $t = 9$, respectively, yet only two half-cycles are counted at $t = 3$ and $t = 8$. The original online counting algorithm described in [59] fails to account for the last half-cycle ending at the final time step.

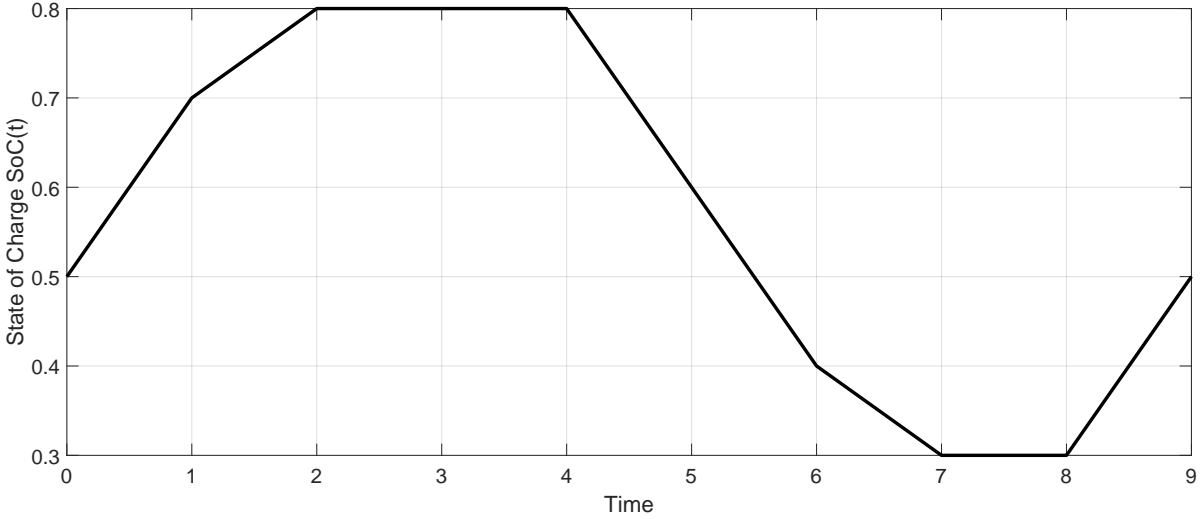


Figure 3.12: An example of SoC profile to illustrate online cycle counting algorithm working principles

Table 3.3: The corresponding continuous and binary variable values of the given SoC example profile

	t	0	1	2	3	4	5	6	7	8	9
Continuous Variables	$SoC(t)$	0.5	0.7	0.8	0.8	0.8	0.6	0.4	0.3	0.3	0.5
	$x(t)$	0.5	0.5	0.5	0.8	0.8	0.8	0.8	0.8	0.3	0.3
	$c(t)$	0	0.2	0.1	0	0	0	0	0	0	0.2
	$d(t)$	0	0	0	0	0	0.2	0.2	0.1	0	0
	$DoD(t)$	0	0	0	0.3	0	0	0	0	0	0.5
Binary Variables	$Z^{chg}(t)$	0	1	1	0	0	0	0	0	0	1
	$Z^{dis}(t)$	0	0	0	0	0	1	1	1	0	0
	$Z_{st}^{chg}(t)$	0	1	0	0	0	0	0	0	0	1
	$Z_{end}^{chg}(t)$	0	0	0	1	0	0	0	0	0	0
	$Z_{st}^{dis}(t)$	0	0	0	0	0	1	0	0	0	0
	$Z_{end}^{dis}(t)$	0	0	0	0	0	0	0	0	1	0
	$Z^{CC}(t)$	0	0	0	1	0	0	0	0	1	0

To account for half-cycles that ends at the final time step, the following constraints are added to the original online counting algorithm:

$$DoD(t_{end}) \geq SoC(t_{end}) - x(t_{end} - 1) \quad (3.33a)$$

$$DoD(t_{end}) \geq -SoC(t_{end}) + x(t_{end} - 1) \quad (3.33b)$$

3.5. Simulation

3.5.1. Workflow

After formulating the objective function and incorporating constraints, the battery profitability can be analyzed using the workflow depicted in Figure 3.13. Initially, the battery aging model parameters are input into the model during the initialization phase. Subsequently, the daily optimization is executed iteratively until the battery reaches its end-of-life.

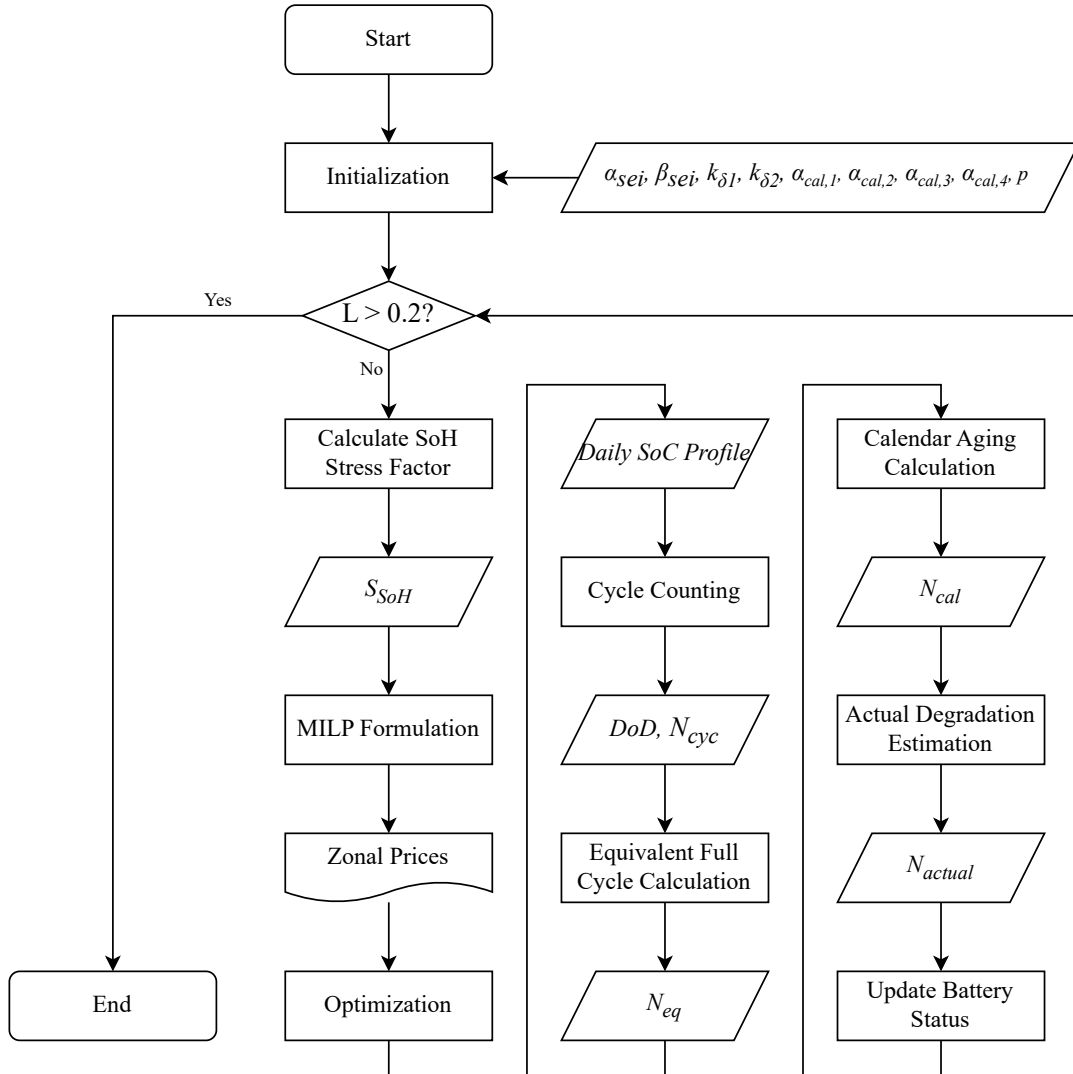


Figure 3.13: Flowchart of the profitability assessment

In each iteration, the SoH stress factor S_{SoH} is calculated using Equation 3.8, based on the current battery SoH, to account for the varying damage that a same cycle will cause to the battery at different SoH. The non-linear degradation process due to operational patterns (DoD) and storage conditions (SoC and temperature) is then formulated within the MILP model as discussed in the subsection 3.3.4. Once the optimal charging/discharging and transportation schedule for the day is determined, the cyclic and calendar aging are estimated using semi-empirical degradation models based on the daily SoC profile. Following the damage estimation, the battery SoH status is updated, and a new iteration begins.

3.5.2. Parameters

The values of the semi-empirical degradation model parameters used in this simulation are provided in Table 3.4 and Table 3.5. The parameters for calendar degradation are sourced from [52], and the cyclic degradation parameters are obtained from [42]. The system operation parameters are listed in Table 3.6.

Table 3.4: Calendar degradation parameters

Parameter	$\alpha_{cal,1}$	$\alpha_{cal,2}$	$\alpha_{cal,3}$	$\alpha_{cal,4}$	p
Value	3.00×10^{-4}	0.53	-2.70	-1.02	0.52

Table 3.5: Cyclic degradation parameters

Battery	Parameter	Value	Battery	Parameter	Value
<i>LFP</i>	α_{sei}	3.14×10^{-2}	<i>LMO</i>	α_{sei}	5.75×10^{-2}
	β_{sei}	9.51×10		β_{sei}	1.21×10^2
	$k_{\delta,1}$	2.02×10^{-5}		$k_{\delta,1}$	1.40×10^5
	$k_{\delta,2}$	5.73×10^{-1}		$k_{\delta,2}$	-5.01×10^{-1}
			$k_{\delta,3}$	-1.23×10^5	

Table 3.6: System operation parameters

Symbol	Definition	Unit	Value
c^T	Transportation Cost	[€/h]	22
c^D	LFP Throughput Degradation Cost	[€/MWh]	14
c^D	LMO Throughput Degradation Cost	[€/MWh]	16
d_{12}, d_{21}	Transportation Time NO1,2	[h]	1
d_{13}, d_{31}	Transportation Time NO1,3	[h]	5
d_{23}, d_{32}	Transportation Time NO2,3	[h]	6
L_{eol}	End of Life Capacity Loss	[-]	0.2
M	Big M for if-else Condition	[-]	3
r	Yearly Discount Rate	[-]	0.05
SoC_{sto}	Storage SoC	[-]	0.5
T_{sto}	Storage Temperature	[°C]	25

In Table 3.6, the throughput costs per MWh of energy for LFP and LMO batteries are set at €14 and €16, respectively, generating the highest lifetime net present value (NPV). Simulation results using alternative values are provided in Appendix A.

3.5.3. Price Input Adjustment

One limitation of the portable energy storage system (PESS) model presented in this study is its inability to capture long-term price trends, because the optimization horizon is 24 hours instead of a year. Consequently, the model will demonstrate the following behavior: assuming that the PESS parking base is located in bidding zone NO5, near the border of bidding zone NO3, the price difference between these two zones during spring, summer and winter makes spatial-temporal arbitrage highly profitable. While in autumn, the price difference between NO5 and NO2 surpasses that between NO5 and NO3 for most of the season, indicating that the PESS should relocate its parking base within NO5 to a node closer to the NO2 border. However, the daily optimization does not accommodate this parking base movement, since it is not the most profitable schedule for any specific day.

Taking this limitation into account, the price input in this study is manually adjusted based on the original data to enhance the profitability. The price data of bidding zone NO3 from day 196 to day 282 is replaced with the price in bidding zone NO2 for the corresponding days, indicating the parking base movement. The original NO2, NO3 price data and adjusted price data $NO_{2\&3}$ are presented in Figure 3.14.

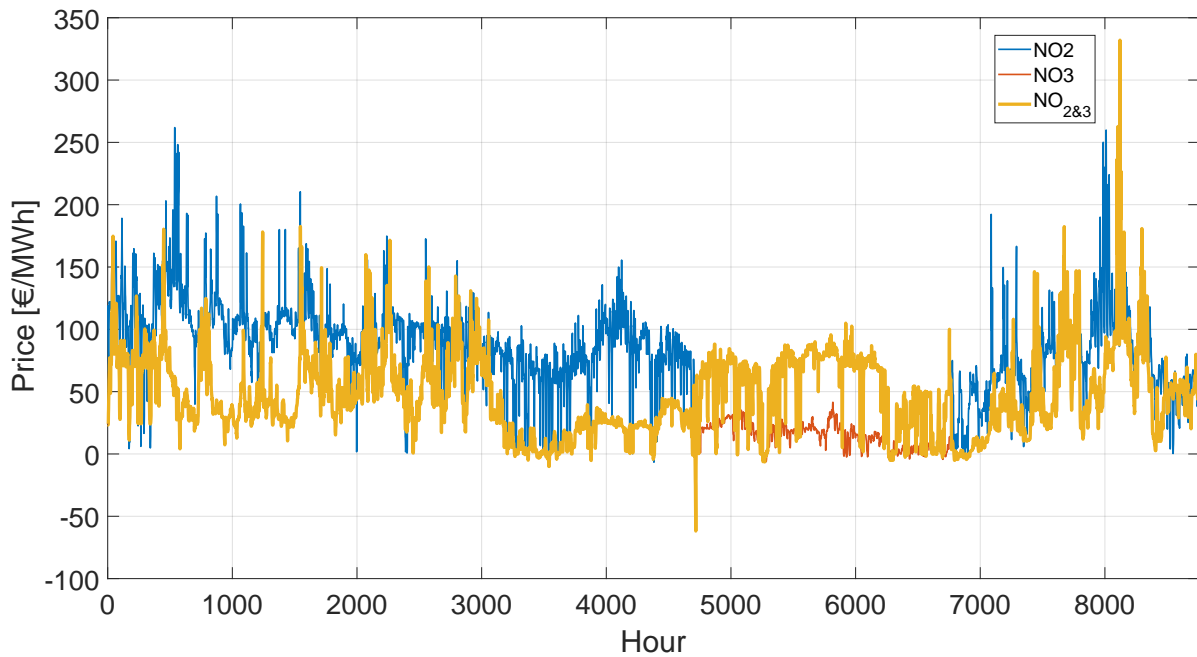


Figure 3.14: The hourly day-ahead electricity tariff $NO_{2\&3}$ used in the simulation

3.6. Chapter Summary

In this chapter, we present the input price signal of the model, the system composition, and the values of rating and costs for each element in the system. The revenue and traveling cost terms in the objective function are formulated, along with degradation cost terms using two distinct degradation models: the energy throughput model and the semi-empirical model. The latter encourages the battery to operate with a cycle depth between 0.3 and 0.4. Furthermore, model constraints for operation, transport, and online cycle counting are introduced to determine the feasible domain and solution space of the mixed integer linear programming (MILP) model.

After constructing the model, the profitability assessment workflow is presented, along with the parameters used in the simulation. Before running the simulation, it is essential to note the following simplifications have been assumed, for the battery itself:

1. Self-discharge is neglected.
2. Battery SoH within a day is considered constant.
3. Charging and discharging actions are doing equal amount of damage to battery SoH.
4. Cyclic degradation rate is only related to its operation pattern and is independent of current SoH.
5. Only the energy capacity fade is considered, there is no power capacity fade.

For operational conditions:

1. Perfect electricity price foresight is assumed and the PESS is a price-taker.
2. The transportation cost is a constant value €22/h during the whole battery life span.
3. There is no traffic jam or maintenance, travel time between nodes are constant forth and back.
4. The battery temperature is considered constant at 25°C.
5. The daily initial and final locations of the PESS are the same.
6. The daily initial and final SoC levels of the PESS are the same.

4

Results

After running the simulation iteratively until the end of battery life with two different degradation models, the simulation results for stationary energy storage system (SESS) and portable energy storage system (PESS) are presented in this chapter.

4.1. Stationary Energy Storage System: LFP Battery

This section aims at analyzing the profitability of the stationary energy storage system. To this end, we will analyze the profitability of stationary energy storage systems (SESSs) in two distinct bidding zones, NO1 and NO2. The power and energy capacity of SESSs will be the same as those of PESSs, which are 1.2 MW and 3 MWh, respectively.

4.1.1. LFP: Degradation Comparison

To ensure consistency of units of measure, the calendar degradation is converted from percentage to number of equivalent full cycles. The varying calendar degradation slope over battery life time in this figure can attribute to the fact that same percentage of capacity loss corresponds to different number of full cycles at different battery SoH.

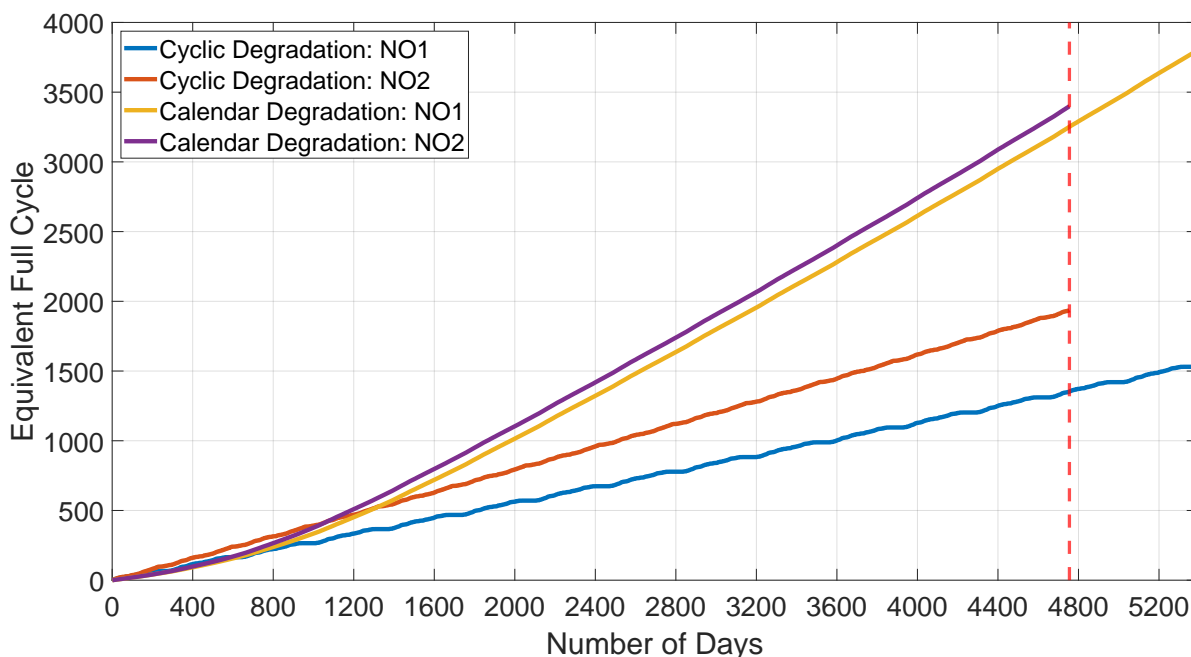


Figure 4.1: The damage measured in equivalent full cycle in bidding zone NO1 and NO2

Figure 4.1 presents the degradation caused by cyclic aging and calendar aging at a daily initial SoC of 0.5. Due to significantly shorter simulation times, only the results using the energy throughput model are given here. As can be seen, battery in bidding zone NO2 first reaches its end of life due to its more frequent charging and discharging actions, indicating that bidding zone NO2 has a higher temporal price volatility than that of bidding zone NO1.

4.1.2. LFP: Revenue and Net Present Value Comparison

Notably, calendar ageing played a dominant role in stationary battery system ageing. Which means the battery lost most of its capacity without any income, resulting in low profitability. And the yearly revenue and end-of-year SoH in bidding zone NO1 and NO2 are presented in Figure 4.2.

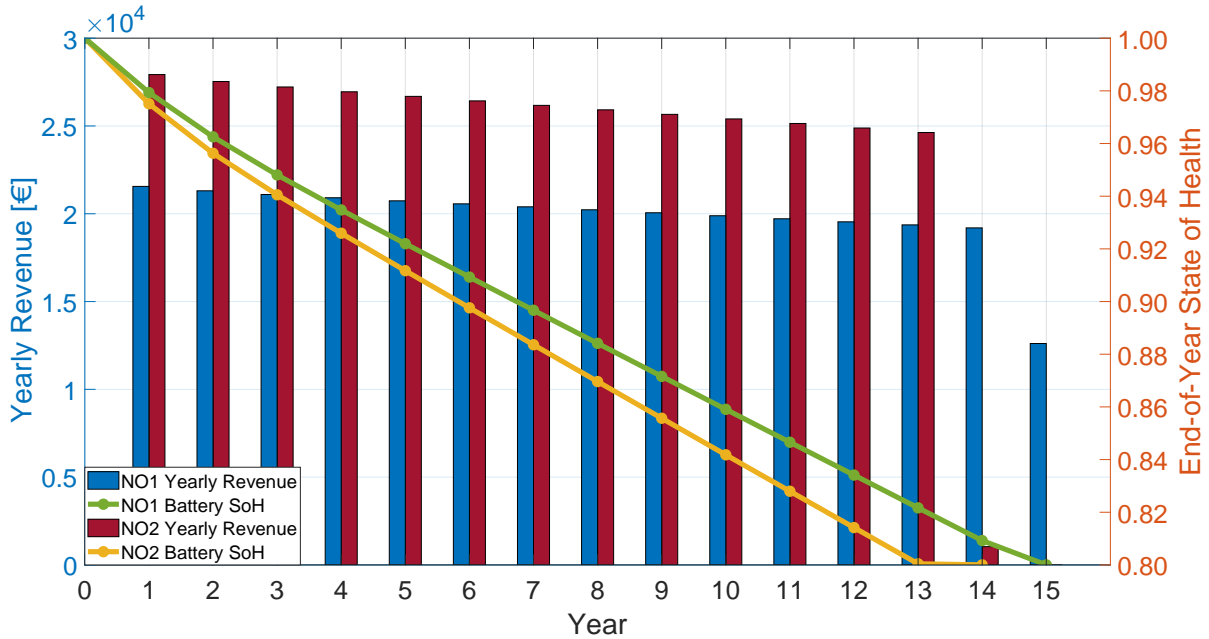


Figure 4.2: The yearly revenue and state of health of the SESS in bidding zone NO1 and NO2

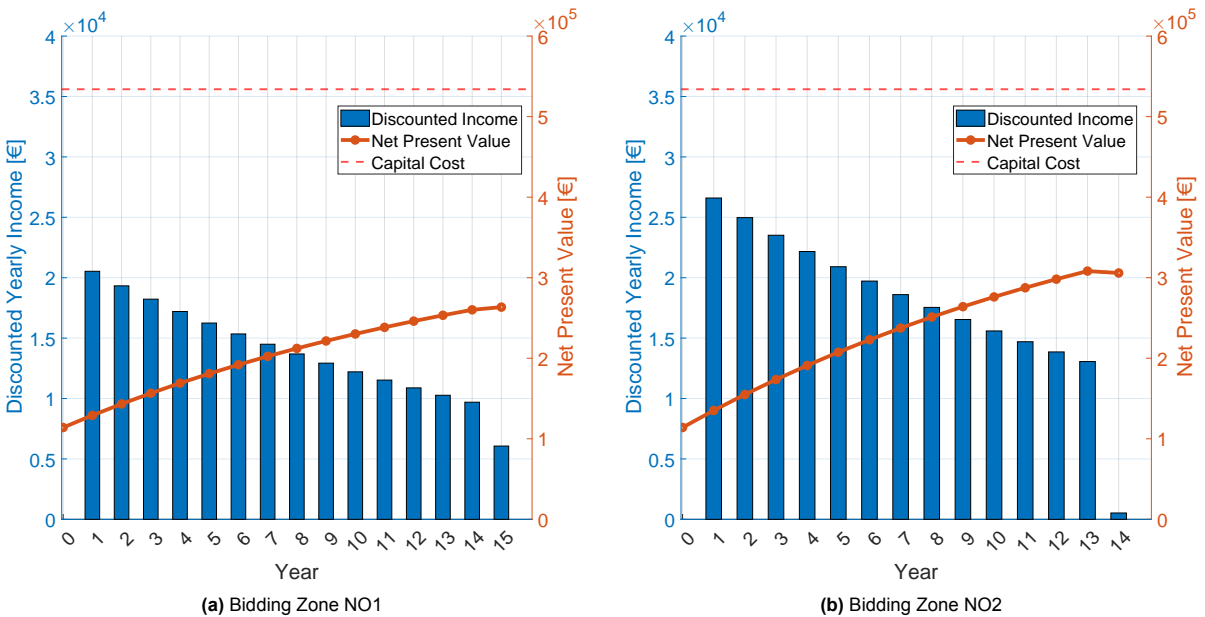


Figure 4.3: Comparison between the discounted revenue and net present value in bidding zone NO1 and NO2

Considering the time value of money, a yearly discount rate $r = 5\%$ is used to account for factors like inflation. The discounted income and net present value results are presented in Figure 4.3.

4.2. Stationary Energy Storage System: LMO Battery

4.2.1. LMO: Degradation Comparison

Figure 4.4 presents the battery degradation results caused by cyclic aging and calendar aging.

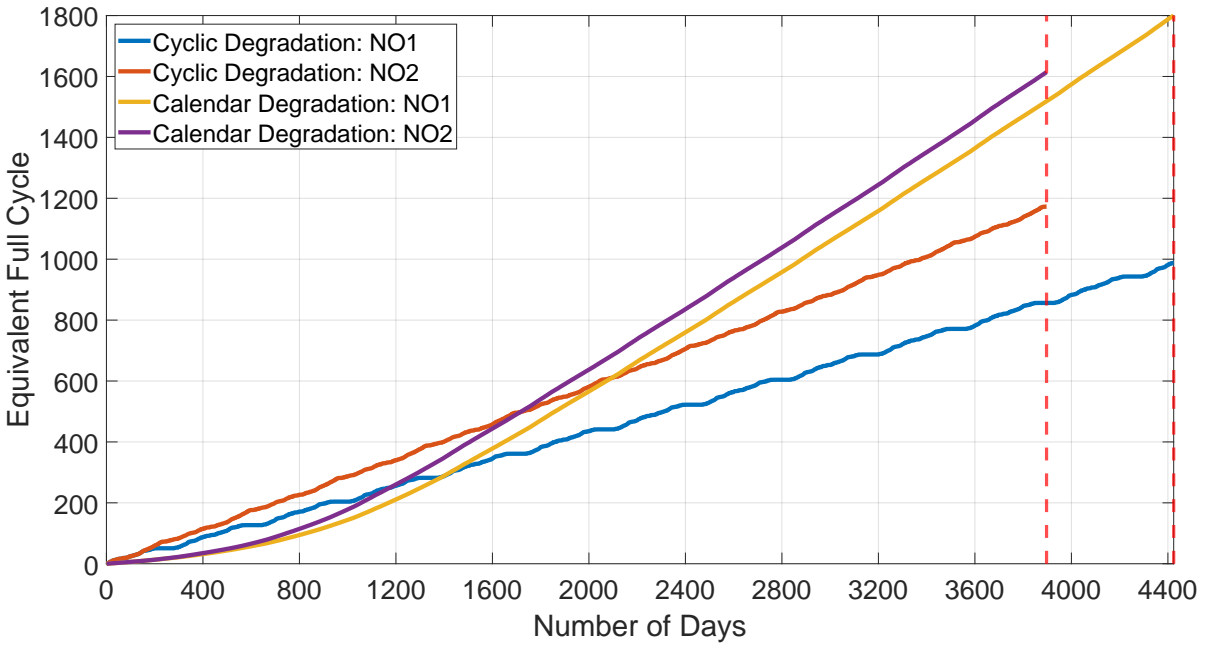


Figure 4.4: The damage measured in equivalent full cycle in bidding zone NO1 and NO2

4.2.2. LMO: Revenue and Net Present Value Comparison

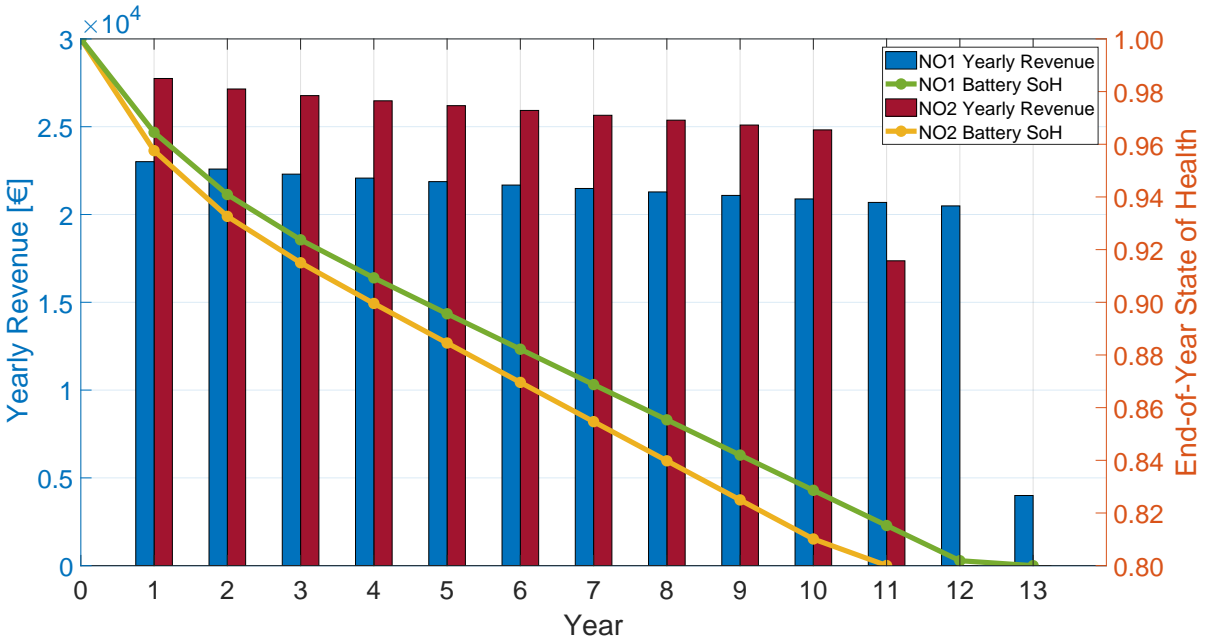


Figure 4.5: The yearly revenue and state of health of the SESS in bidding zone NO1 and NO2

Figure 4.5 presents the yearly revenue and battery SoH over battery service life. After considering the 5% yearly discount rate, the discounted revenue and system net present value results are presented in Figure 4.6.

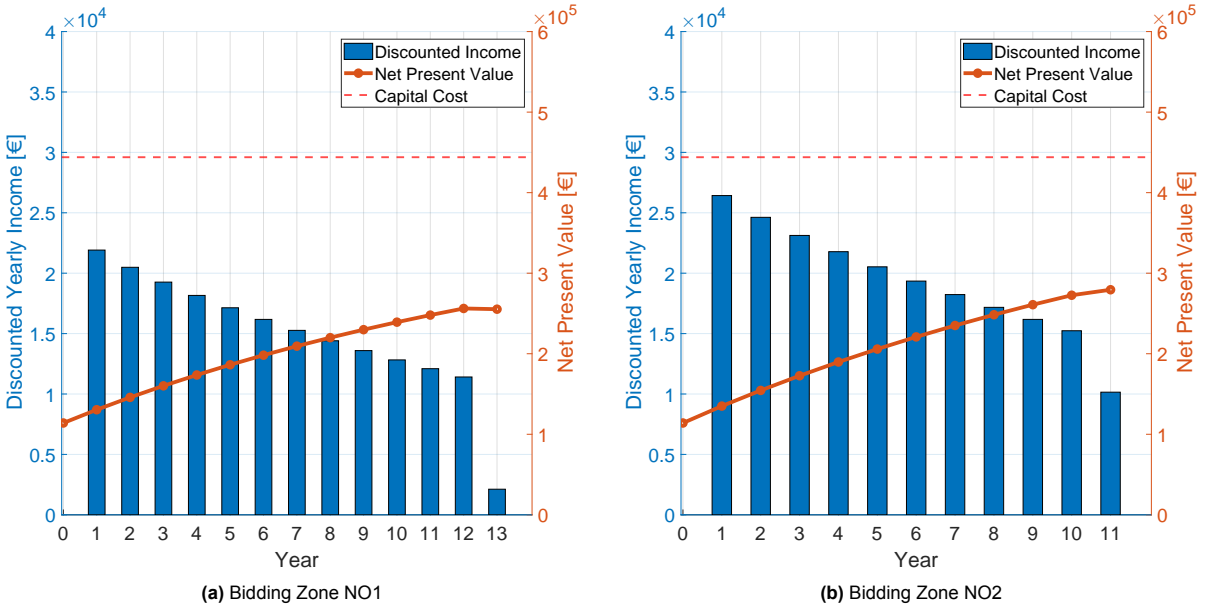


Figure 4.6: Comparison between the discounted revenue and net present value in bidding zone NO1 and NO2

Table 4.1 provides detailed simulation results for various stationary systems with different battery chemistry, across different bidding zones as presented in section 4.1 and section 4.2. The simulation results of stationary battery systems in other bidding zones are provided in Table A.3 and Table A.4 in Appendix A.

Table 4.1: Comparison of the degradation and profitability in bidding zone NO2 and NO5

Bidding Zone	Battery Chemistry	Equivalent Full Cycle Number (Cyclic)	Equivalent Full Cycle Number (Calendar)	Battery Service Life [day]	Net Present Value [€]	Investment Cost [€]
NO1	LFP	1,936	3,397	5,394	263,475	534,000
	LMO	988	1,800	4,424	255,307	444,000
NO2	LFP	1,532	3,802	4,755	305,883	534,000
	LMO	1,173	1,614	3,897	279,450	444,000

The presented data indicate that none of the four examined stationary energy storage systems (SESSs) achieve break-even. This outcome can be attributed to the low temporal tariff volatility within all bidding zones, resulting in the battery remaining idle for much of its service life rather than engaging in arbitrage. Consequently, calendar degradation occurs as majority without generating profit. Furthermore, all four proposed systems have service lives that are longer than 10 years, leading to a significant diminishing in actual value during the later years of the battery’s lifespan.

4.3. Relocatable Energy Storage System: LFP Battery

4.3.1. LFP: Degradation Comparison

The degradation results with different LFP battery degradation models are given in Figure 4.7.

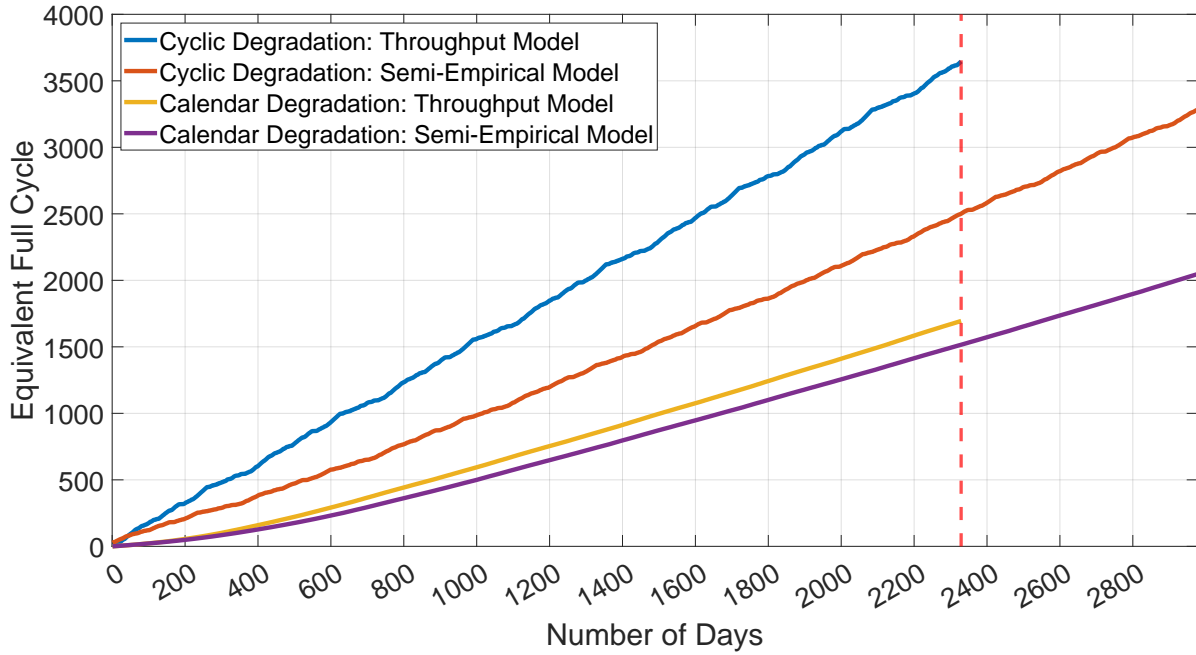


Figure 4.7: The damage measured in equivalent full cycle with different degradation models

As illustrated in Figure 4.7, the system with semi-empirical degradation model exhibits relatively slower growth rates in both cyclic and calendar aging compared to the system with energy-throughput model. Consequently, the system with the energy-throughput model reaches its end of life sooner. Due to its shorter service life, cyclic aging constitutes a higher percentage than in energy throughput model.

4.3.2. LFP: Revenue and Net Present Value Comparison

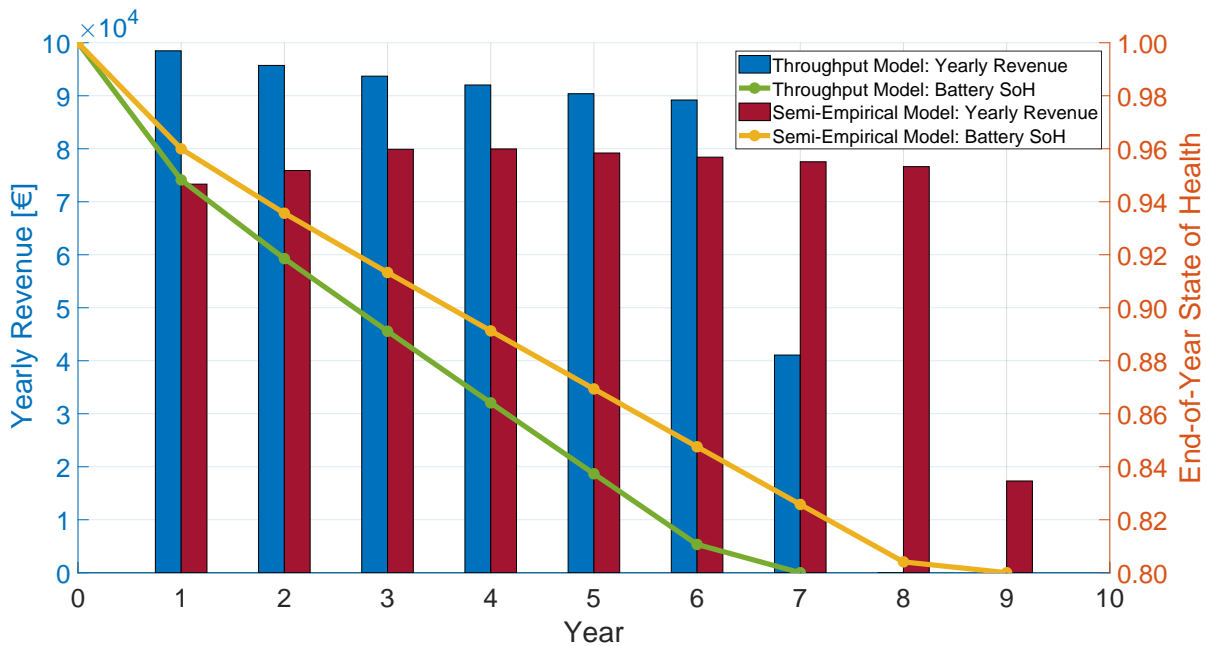


Figure 4.8: The yearly revenue and state of health of the PESS with different degradation models

The annual revenue and battery SoH at the end of each year are illustrated in Figure 4.8. Over the initial six-year period, the energy throughput model yields higher revenues, depleting the battery capacity by the seventh year. Conversely, although the semi-empirical model generates lower annual revenues during these first six years, it continues to produce income until the ninth year.

Taking into account the time value of money, the discounted annual income and net present value (NPV) of the PESS with two distinct degradation models are depicted in Figure 4.9. As illustrated, both degradation models of PESSs demonstrate profitability.

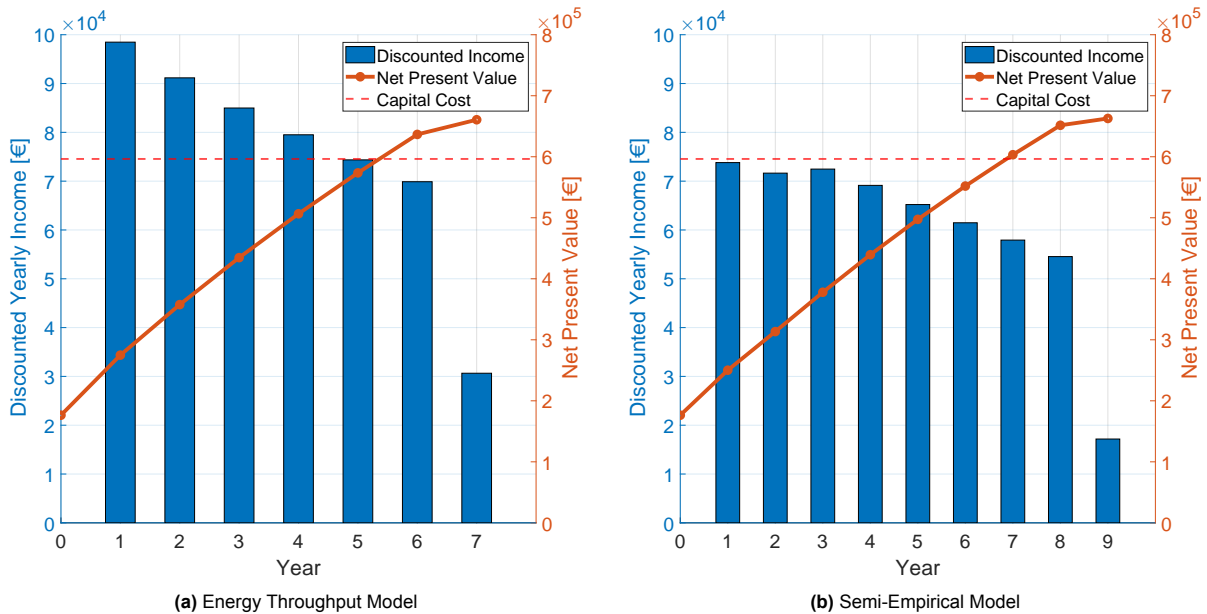


Figure 4.9: Comparison between the discounted revenue and net present value

The detailed simulation results of degradation and profitability are presented in Table 4.2.

Table 4.2: Comparison of the degradation and profitability with different models

Degradation Model	Service Life [day]	Pay-Back Period [day]	Lifetime Revenue [€]	Net Present Value [€]	Investment Cost [€]	Investment Return Rate
Semi-Empirical	3,005	2,498	646,427	662,773	596,400	11.13%
Energy Throughput	2,329	1,954	600,584	660,658	596,400	10.77%

As shown in Table 4.2, the semi-empirical model extends battery service life and improves both system lifetime revenue and net present value (NPV). The lifetime revenue has increased by over 6% compared to the energy throughput model; however, the net present value and investment return rate see a modest rise of only 0.36%, with a 544-day longer payback period.

This outcome can be attributed to the optimization model's focus on maximizing daily profit rather than lifetime NPV, coupled with the time value of money. Although the semi-empirical model boosts lifetime revenue by over 6%, the discounted value of revenues in years 8 and 9 diminishes significantly over time. This suggests that, in this scenario, the advantages of extending battery service life with a conservative strategy do not substantially outweigh those of a more aggressive approach.

For a more detailed analysis, the revenue, travel cost, degradation cost and profit of both systems are presented in Figure 4.10. It is noteworthy that the relocatable energy storage system is actually losing money during the first year due to the high cycle degradation cost, which can be explained by the rapid cyclic aging caused by solid electrolyte interphase (SEI) formulation as shown in Figure 2.3.

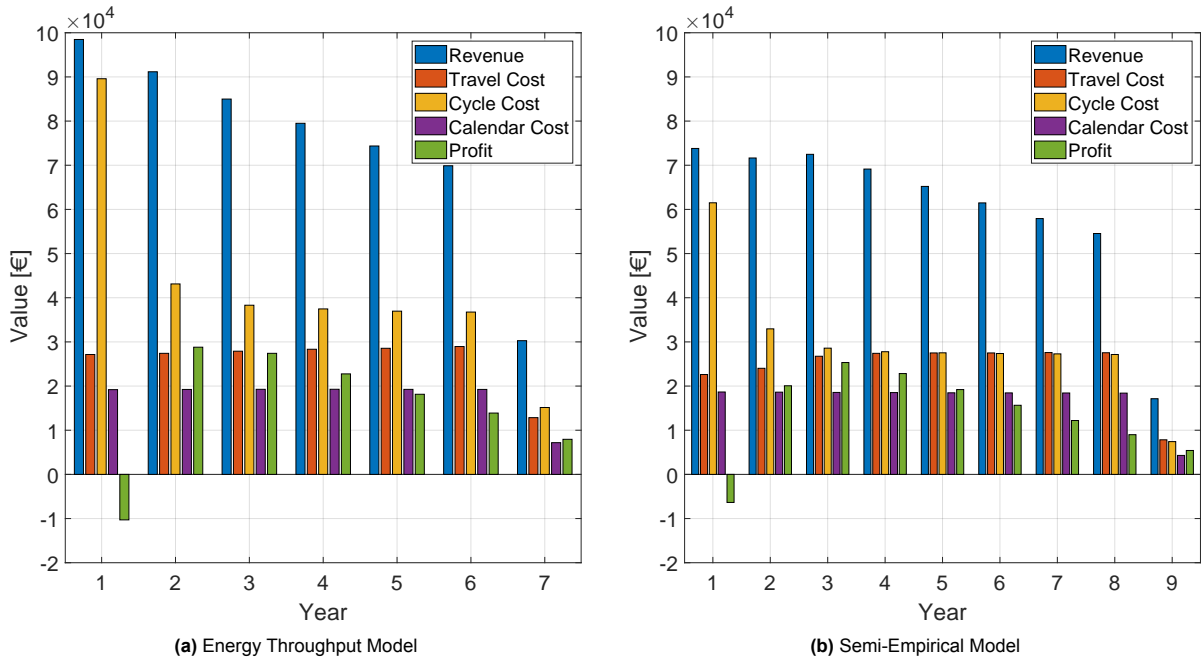


Figure 4.10: Comparison between discounted revenue, travel cost, degradation costs and profit

4.3.3. LFP: Operational Pattern Comparison

The operational patterns of LFP PESSs with different degradation models are compared in this subsection. The histograms of cycle depth value throughout battery lifetime are presented in Figure 4.11.

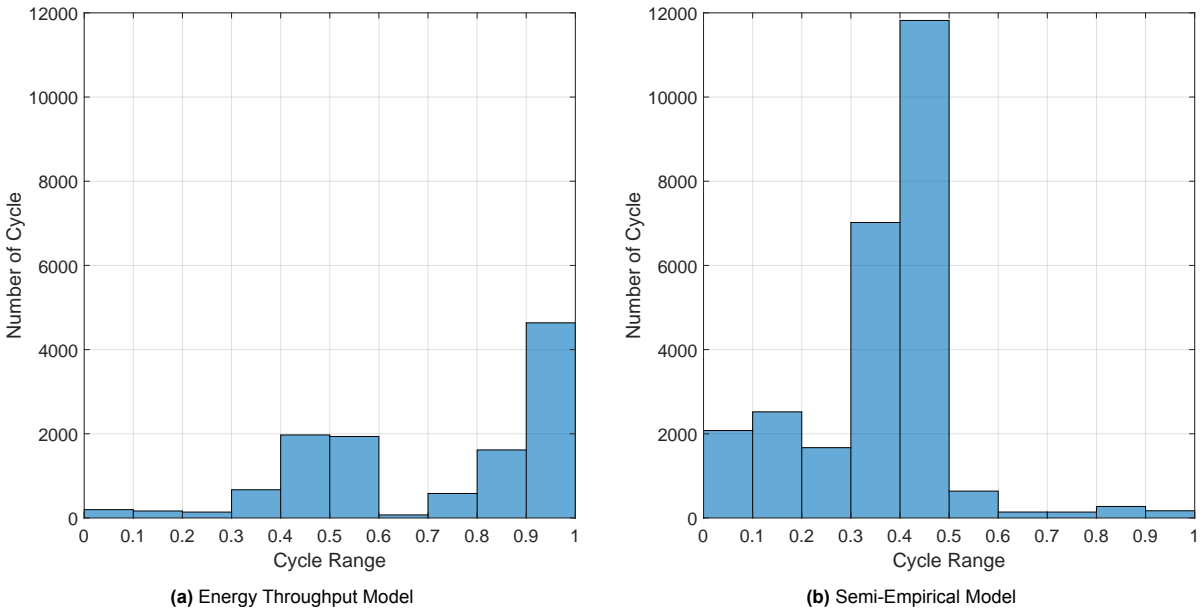


Figure 4.11: Comparison between the cycles distribution histogram throughout battery lifetime

As illustrated in Figure 4.11, the PESS with energy throughput degradation model exhibits a majority of its depth of discharge (DoD) cycles within the range of 0.9 to 1.0. The subsequent most common DoD ranges are 0.4 to 0.6 and 0.8 to 0.9. In contrast, the PESS utilizing the semi-empirical model predominantly cycles within the DoD range of 0.3 to 0.5. Notably, the semi-empirical model encourages more cycles within the 0.3 to 0.5 DoD range, as this interval corresponds to the lowest degradation cost per unit of energy, as depicted in Figure 3.7a.

To compare the calendar degradation, the state of charge (SoC) level distribution histograms are presented in Figure 4.12. As shown, both models exhibit the highest number of hours in the SoC interval from 0.5 to 0.6. However, the semi-empirical model has fewer hours with SoC between 0.9 and 1.0, resulting in a 5% lower average SoC and slower calendar aging rate compared to the energy throughput model as illustrated in Figure 4.7.

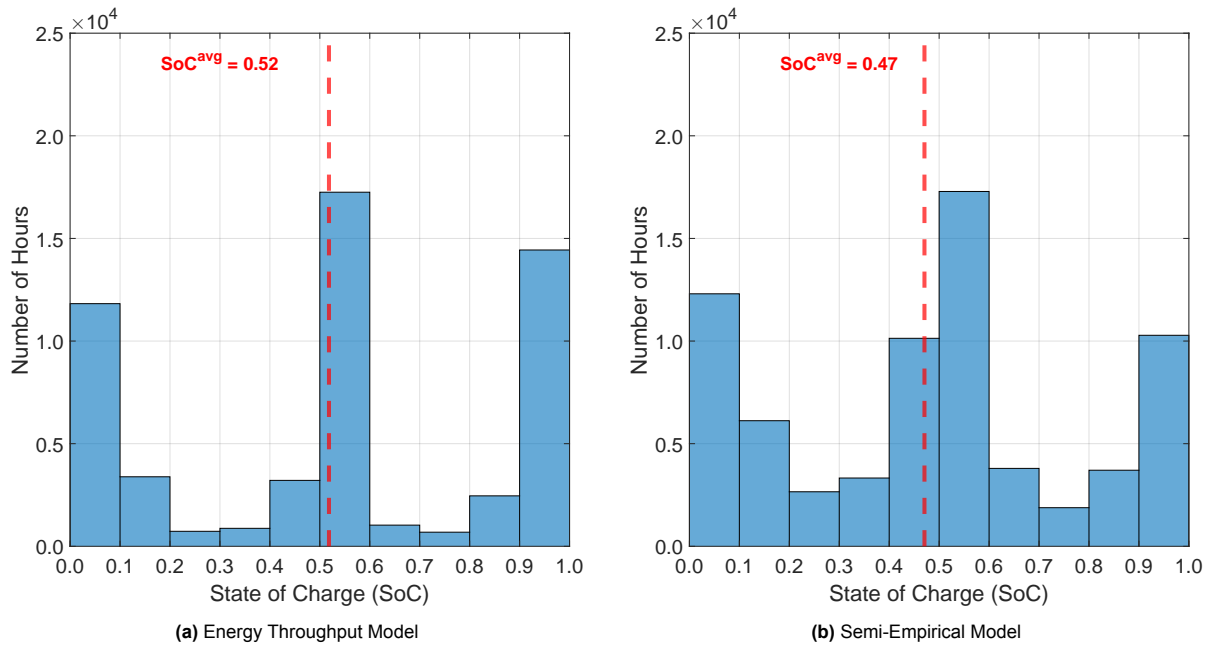


Figure 4.12: Comparison between the SoC level distribution throughout battery life time

4.4. Relocatable Energy Storage System: LMO Battery

4.4.1. LMO: Degradation Comparison

The degradation results with different LMO battery degradation models are given in Figure 4.13.

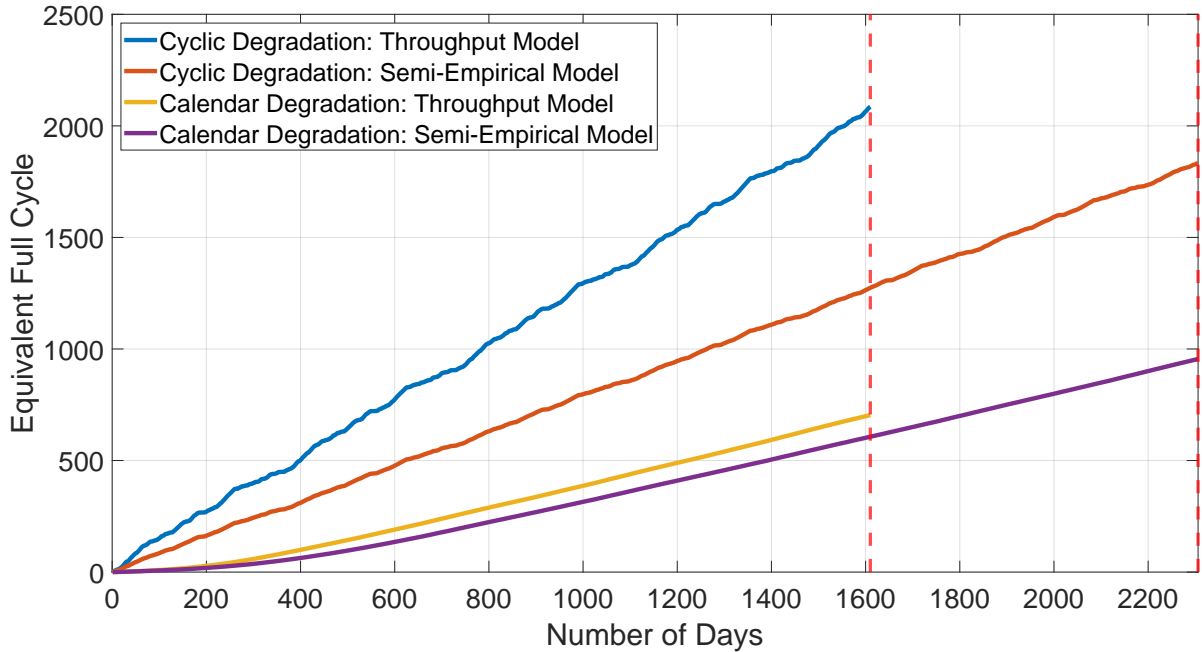


Figure 4.13: The damage measured in equivalent full cycle with different degradation models

As can be seen, the semi-empirical degradation model has extended the system’s service life by over 600 days, which gives a over 40% life-time increase. In this case, both cyclic and calendar degradation rate of semi-empirical model are slower compared to energy throughput model, demonstrating similarity to the LFP batteries.

4.4.2. LMO: Revenue and Net Present Value Comparison

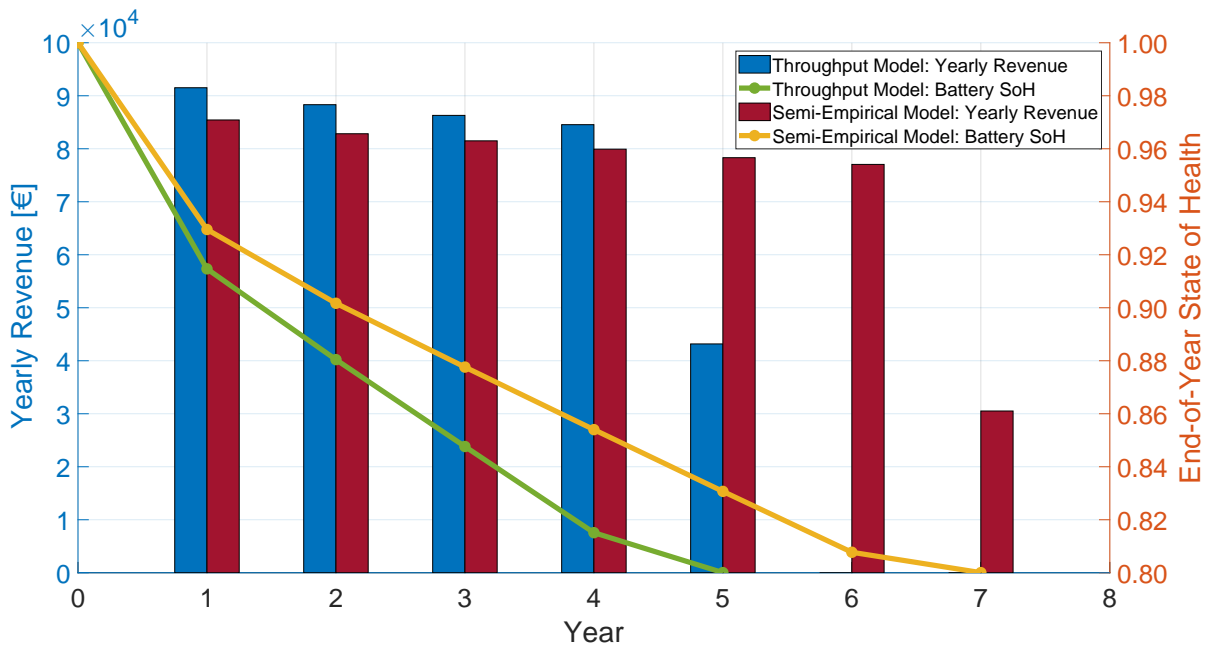


Figure 4.14: The yearly revenue and state of health of the PESS with different degradation models

The revenue and SoH plot in Figure 4.14 showed similarity to that of the LFP battery in Figure 4.8: the system with semi-empirical model generates lower revenue during the initial four years but continues to generate revenue until the seventh year. In contrast, the energy throughput model has already depleted battery life by the end of the fifth year.

The discounted yearly revenue and net present value of both LMO battery systems are compared in Figure 4.15. The detailed simulation results are given in Table 4.3.

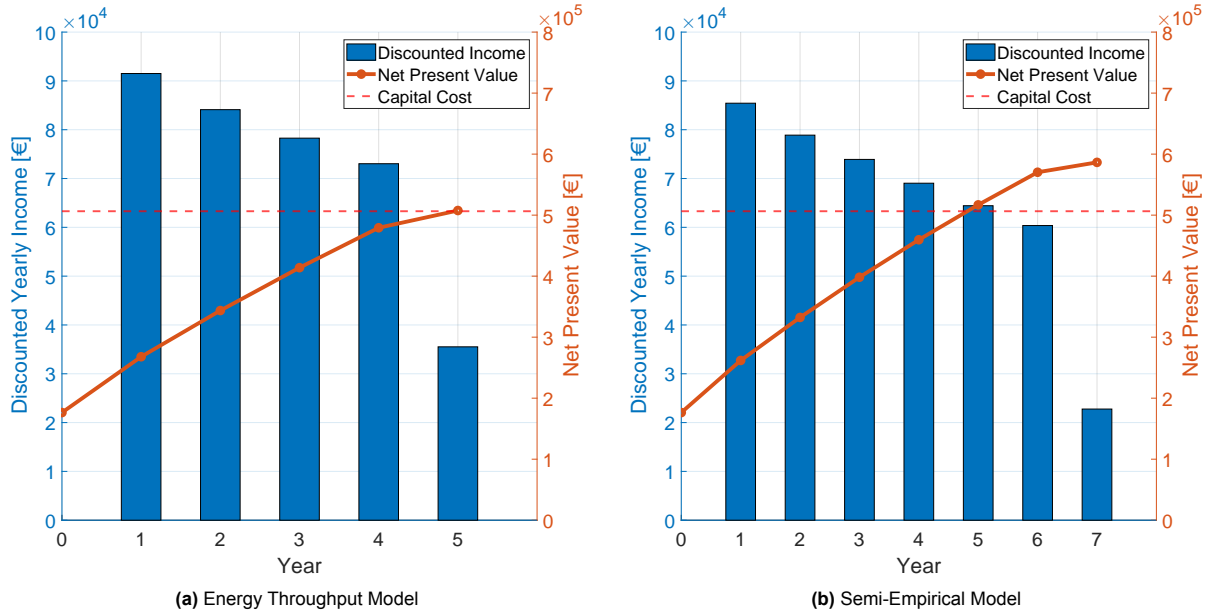


Figure 4.15: Comparison between the discounted revenue and net present value

Table 4.3: Comparison of the degradation and profitability with different models

Degradation Model	Service Life [day]	Pay-Back Period [day]	Lifetime Revenue [€]	Net Present Value [€]	Investment Cost [€]	Investment Return Rate
Semi-Empirical	2,326	1,772	517,738	587,214	506,400	15.96%
Energy Throughput	1,610	1,605	393,839	507,569	506,400	0.23%

As shown, the system with energy throughput model barely achieves break-even, whereas the system with semi-empirical model demonstrates higher profitability. Although the energy throughput model has a comparatively shorter payback period, it reaches the end of service life right after breaking even. In contrast, the semi-empirical model continues to generate revenue beyond the break-even point for more than a year and a half.

In this case, the system profitability is substantially enhanced over a longer life span by employing the semi-empirical degradation model, which is different from the conclusion of LFP battery drawn in subsection 4.3.2. The main reasons are: 1) battery chemistry – compared to LFP battery, LMO battery is significantly more sensitive to high DoD, as illustrated in Figure 3.6, meaning that the benefit of operating the battery within a preferable DoD (0.2 - 0.5 for LMO) outweighs the extra income brought by a larger DoD, and 2) the shorter life span of LMO battery, meaning that the value of revenues in the final years of semi-empirical model is less diminished compared to LFP battery.

In Figure 4.16, the revenue, travel cost, degradation cost and profit of both systems are presented. Similar to the LFP battery, the profit of both systems in the first year are negative. While in contrast to LFP battery, the battery cyclic degradation cost of LMO battery even exceeded the system revenue, which can be attributed to the faster capacity fade of a new LMO battery.

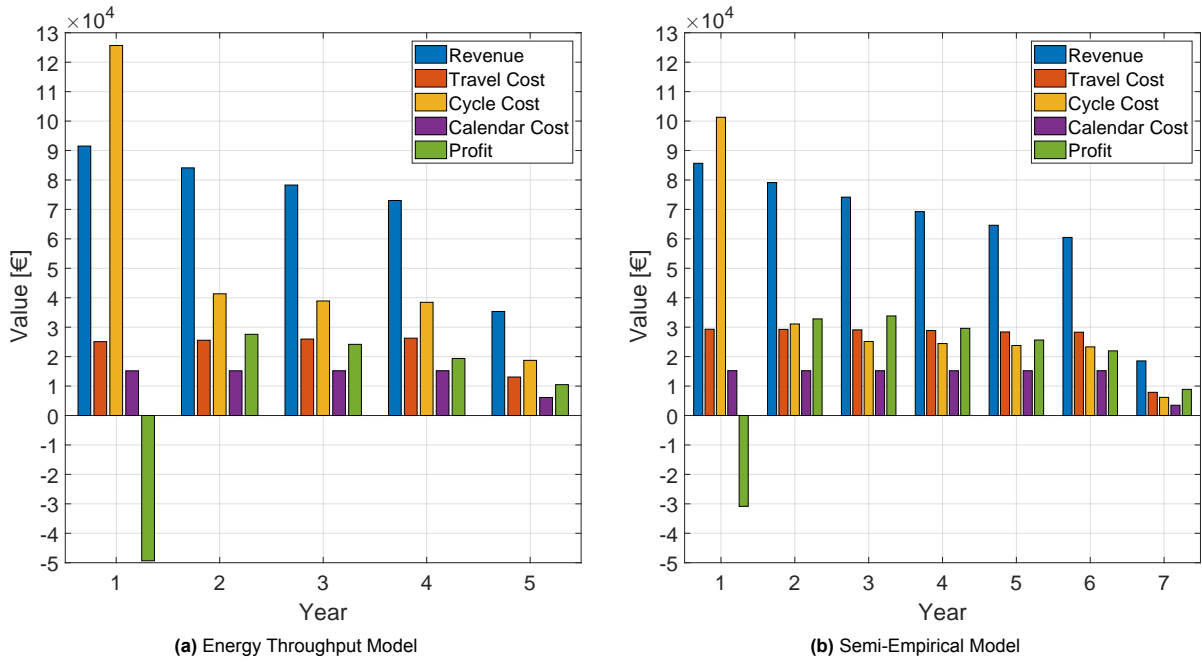


Figure 4.16: Comparison between discounted revenue, travel cost, degradation costs and profit

4.4.3. LMO: Operational Pattern Comparison

The cycle range histograms for systems with both degradation models are presented in Figure 4.17. As shown, the system with the energy throughput model has the majority of its cycle ranges concentrated in the 0.9-1.0 interval, with the next most common ranges being 0.4-0.6 and 0.8-0.9. While the system with the semi-empirical model primarily operates within cycle ranges of 0.3 to 0.5, which corresponds to the high lifetime energy throughput interval depicted in Figure 3.6.

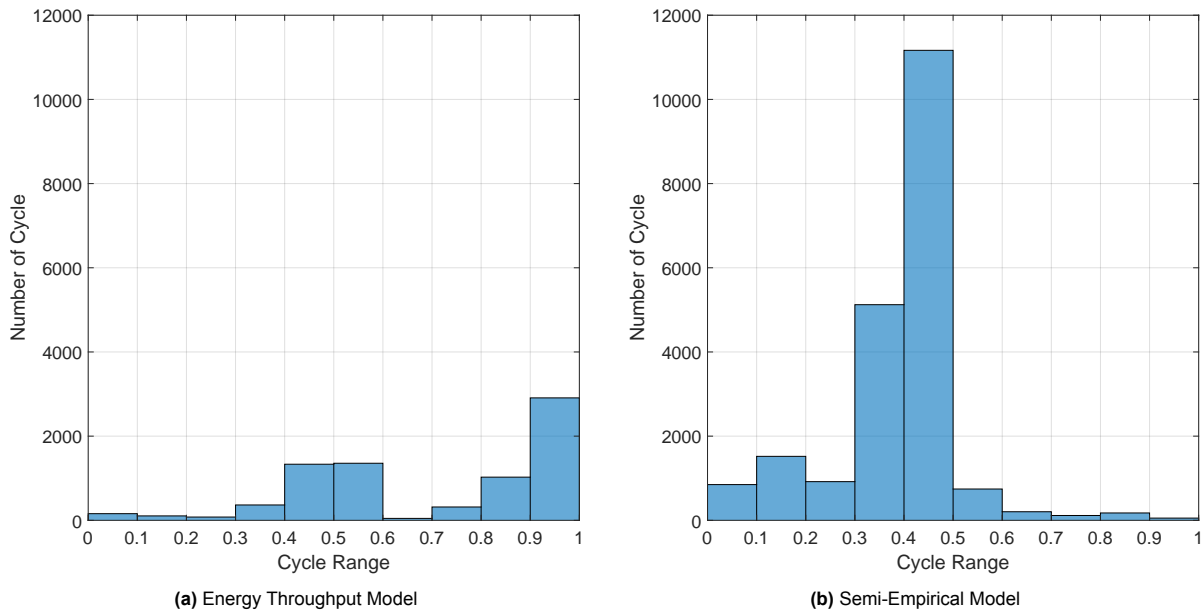


Figure 4.17: Comparison between the cycle range distribution throughout battery life time

Figure 4.18 presents the SoC level distribution for both LMO systems. Both models exhibit the highest number of hours in the 0.5-0.6 SoC interval. However, the system using the semi-empirical model spends more hours in lower SoC intervals, such as 0-0.1 and 0.4-0.5, and fewer hours in the 0.9-1.0 SoC range, leading to a 4% lower lifetime average SoC compared to the energy throughput model.

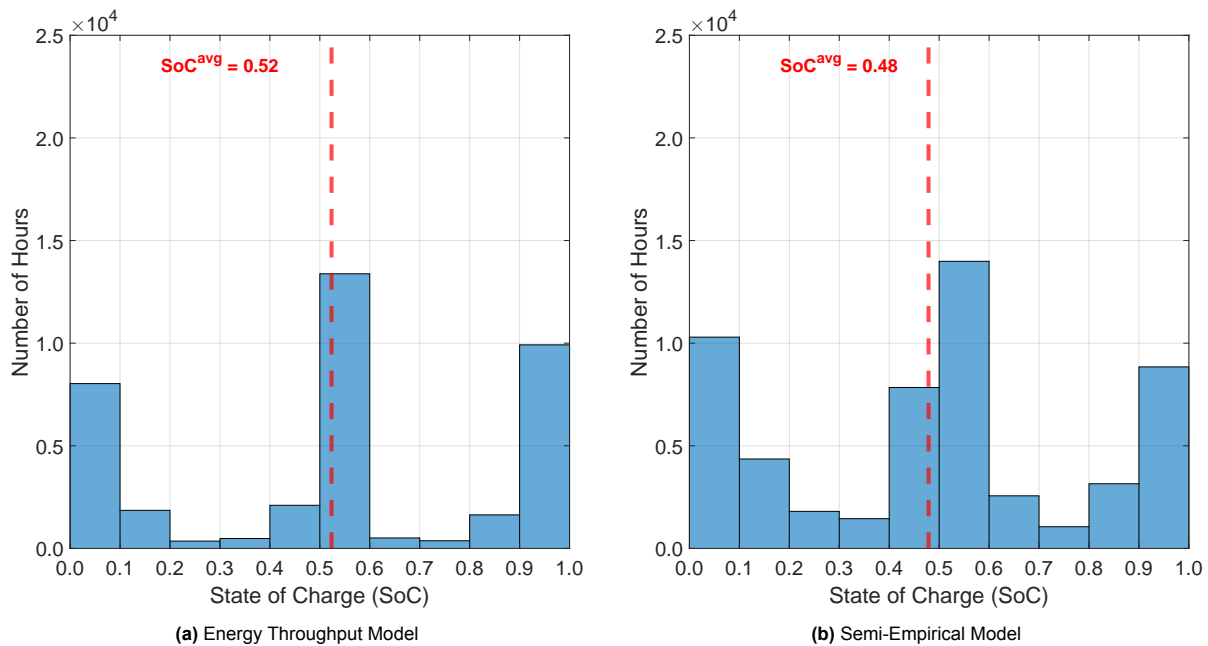


Figure 4.18: Comparison between the SoC level histogram throughout battery lifetime

4.5. Chapter Summary

In this chapter, we present and analyze the simulation results of portable energy storage systems (PESSs) with different degradation models as well as stationary energy storage systems (SESSs) in two different bidding zones.

Some key take-outs for stationary energy storage systems are as follows:

1. Bidding zone NO1 and NO2 have the highest temporal price volatility, and the temporal arbitrage system in NO2 has the highest lifetime net present value (NPV) among all bidding zones.
2. The stationary energy storage systems are not capable of breaking even in any of the Norwegian bidding zones if the portfolio solely consists of temporal energy arbitrage.
3. Calendar degradation plays the dominant role in the battery capacity fade of stationary energy storage systems, which means the battery capacity is mainly depleted without any profit generated.

For portable energy storage systems:

1. All four portable energy storage systems (LFP and LMO battery with different degradation models) are profitable and all four systems have negative profit in the first year.
2. The semi-empirical model improved the life-time total revenue of both LFP and LMO battery systems. However, it only improved the profitability of LMO system, the LFP system with semi-empirical model is not as profitable as that with energy throughput model.
3. For both LFP and LMO battery systems, the semi-empirical model reduced the cyclic aging rate by operating more cycles at the most favorable depth of discharge.
4. For both LFP and LMO systems, the semi-empirical model decreased the calendar aging rate by maintaining the battery at a lower state of charge.

5

Discussion & Conclusion

As concluded in the previous chapter, although the semi-empirical model increases the life-time revenue of both LFP and LMO systems, it ultimately fails to increase the profitability of the LFP system. This is due to the relatively lower revenue generated during the initial years and the reduced value of revenues in the later years.

5.1. Accelerated Cases

In this chapter, several accelerated scenarios are analyzed with the intent to improve system profitability. For reference, the objective function utilized in this study is given by Equation 5.1:

$$obj(x_t) = R(x_t) - C^T(x_t) - S^{SoH} \cdot C^{cyc}(x_t) - C^{cal}(x_t)$$

$$where x_t = [P_n^{dis}(t), P_n^{Chg}(t), \gamma_{nm}(t), \omega_n(t), \alpha_n(t), \beta_n(t), \theta_n(t) \quad \forall n, m \in \Omega, t \in H] \quad (5.1)$$

The concept behind these accelerated scenarios is to deplete the battery life over a shorter duration through a more aggressive strategy, thereby avoiding the diminished value of revenue in the final years of the battery's lifespan. Two approaches are proposed to achieve this: 1).removing the calendar degradation term, and 2).reducing the upper limit of the state-of-health (SoH) stress factor S^{SoH} , as introduced at the end of subsection 3.3.3.

This chapter presents and compares the following cases:

- **Case 1:** The base case, as outlined in the previous chapter.
- **Case 2:** The calendar degradation term $C^{cal}(x_t)$ removed.
- **Case 3:** The upper bond of SoH stress factor S^{SoH} is set to 1.
- **Case 4:** The upper bond of S^{SoH} set to 1, and calendar term is removed.

Table 5.1: Simulation results of base cases and accelerated LFP battery cases

Battery Chemistry	Scenario	Service Life [day]	Pay-Back Period [day]	Lifetime Revenue [€]	Net Present Value [€]	Investment Cost [€]	Investment Return Rate
LFP	Case1	3,005	2,498	646,427	662,773	596,400	11.13%
	Case2	2,957	2,480	635,843	656,126	596,400	10.01%
	Case3	2,915	2,374	637,637	668,043	596,400	12.01%
	Case4	2,852	2,358	630,359	663,368	596,400	11.22%
	Throughput	2,329	1,954	600,584	660,658	596,400	10.77%

Table 5.1 presents the detailed simulation results of the base case and accelerated cases for LFP battery. As can be seen, even the base case has the highest lifetime revenue, case 3 has the highest net present value and the throughput case has the shortest pay-back period.

Table 5.2: Simulation results of base cases and accelerated LMO battery cases

Battery Chemistry	Scenario	Service Life [day]	Pay-Back Period [day]	Lifetime Revenue [€]	Net Present Value [€]	Investment Cost [€]	Investment Return Rate
<i>LMO</i>	Case1	2,326	1,772	517,738	587,214	506,400	15.96%
	Case2	2,254	1,720	511,142	583,615	506,400	15.24%
	Case3	2,289	1,733	515,145	586,370	506,400	15.79%
	Case4	2,275	1,734	511,326	583,526	506,400	15.23%
	Throughput	1,610	1,605	393,839	507,569	506,400	0.23%

Table 5.2 presents the detailed simulation results of the base case and accelerated cases for LMO battery. In contrast to the LFP battery, even the accelerated cases can shorten the pay-back period, they cannot improve the system net present value.

5.2. Research Questions

Research Question 1: Is the proposed PESS model profitable in general?

As shown in Figure 4.9 and Figure 4.15, despite the LMO battery PESS with energy throughput model can barely break even, all the PESSs presented in this study exhibit profitability under the assumptions outlined in section 3.6.

Research Question 2: Is the proposed PESS model more profitable than SESS model?

As demonstrated in Figure 4.3 and Figure 4.6, none of the proposed stationary energy storage systems (SESSs) in any Norwegian bidding zones are able to break even. In contrast, all four proposed portable energy storage systems PESSs, utilizing different battery chemistries and degradation models, exhibit profitability. Thus, it can be concluded that the proposed PESS is more profitable than the SESS.

Research Question 3: How will the battery chemistry and degradation model influence the spatial-temporal arbitrage profitability?

In general, the energy throughput model aims at maximizing the daily energy arbitrage profit by employing a less accurate cyclic degradation model and disregarding calendar degradation. In contrast, the semi-empirical model takes into account the effect of operational patterns, including depth of discharge (DoD) and state of charge (SoC), and maximizes the overall daily profit by quantifying both cyclic and calendar degradation.

For both LFP and LMO battery systems, integrating the semi-empirical model into the optimization process results in an extended battery service life, increased lifetime total revenues and higher net present value compared to energy throughput model.

The reason why semi-empirical model cannot guarantee a significant increase in lifetime net present value regardless of battery chemistry is because of the optimization horizon of the model. Since the system solely participates in the day-ahead electricity market, the optimization horizon is 24 hours instead of the entire battery service life. This constraint arises from the availability of day-ahead electricity prices, which are only accessible for the subsequent day.

For the LFP battery, characterized by a longer lifespan and lower sensitivity to DoD, the application of the semi-empirical model can optimize the overall daily profit and extend battery life by primarily operating at a DoD of 0.3-0.5 while maintaining a lower SoC. However, the additional discounted revenues generated in the later years of battery life do not substantially outweigh the higher revenues achieved through a more aggressive approach (the energy throughput model) during the earlier stages of battery life. Additionally, due to its more aggressive charging/discharging strategy, the energy throughput model provides a shorter payback period at the cost of an increased degradation rate. Consistent with this observation, the accelerated case 3, where the upper bound of the SoH stress factor S^{SoH} is set to 1, yields the highest net present value.

For the LMO battery, characterized by a relatively shorter lifespan and higher sensitivity to DoD, significant benefits are observed when operating at a DoD of 0.3-0.5. By applying the semi-empirical model, the investment return rate increases from less than 1% to 15.96%. As illustrated in Figure 4.15 and Figure 4.16, although the semi-empirical model generates lower revenue than the energy throughput model during the initial years, its overall yearly profit surpasses that of the energy throughput model over the battery's entire lifespan due to substantially lower cyclic degradation costs. Unlike the LFP battery cases, accelerating the battery's degradation by adjusting the calendar term or the SoH stress factor S^{SoH} does not improve the system's net present value; the base case yields the highest NPV and investment return rate among all scenarios.

In conclusion, the LMO battery portable energy storage system, when incorporating the semi-empirical model, is a more favorable option for spatial-temporal arbitrage. This preference is attributed to its lower investment cost, shorter payback period, and higher investment return rate.

5.3. Further Discussion: Travel and Charging/Discharging Pattern

The previous sections of this study addressed the three research questions, with a focus on analyzing the profitability of the Portable Energy Storage System (PESS). In addition, this section provides several examples to look into the system's transportation and charging/discharging patterns.

5.3.1. Long-term Operation Pattern

As illustrated in Figure 3.14, the PESS is assumed to change its base location from day 196 to day 282 once every year for a higher price volatility, with the corresponding price signal adjusted accordingly. During this period, the PESS engages in spatial-temporal energy arbitrage between bidding zones NO5 and NO2. During the rest of the year, the system operates between NO2 and NO3.

Figure 5.1 and Figure 5.2 presents the charging, discharging, and energy transportation direction of both LFP and LMO battery PESSs over their entire lifespan. Similar operational pattern is observed that: during spatial-temporal arbitrage between NO5 and NO3, the PESS predominantly charges in NO3 and discharges in NO5. While during arbitrage between NO5 and NO2, NO5 becomes the charging zone, while NO2 serves as the discharging zone.

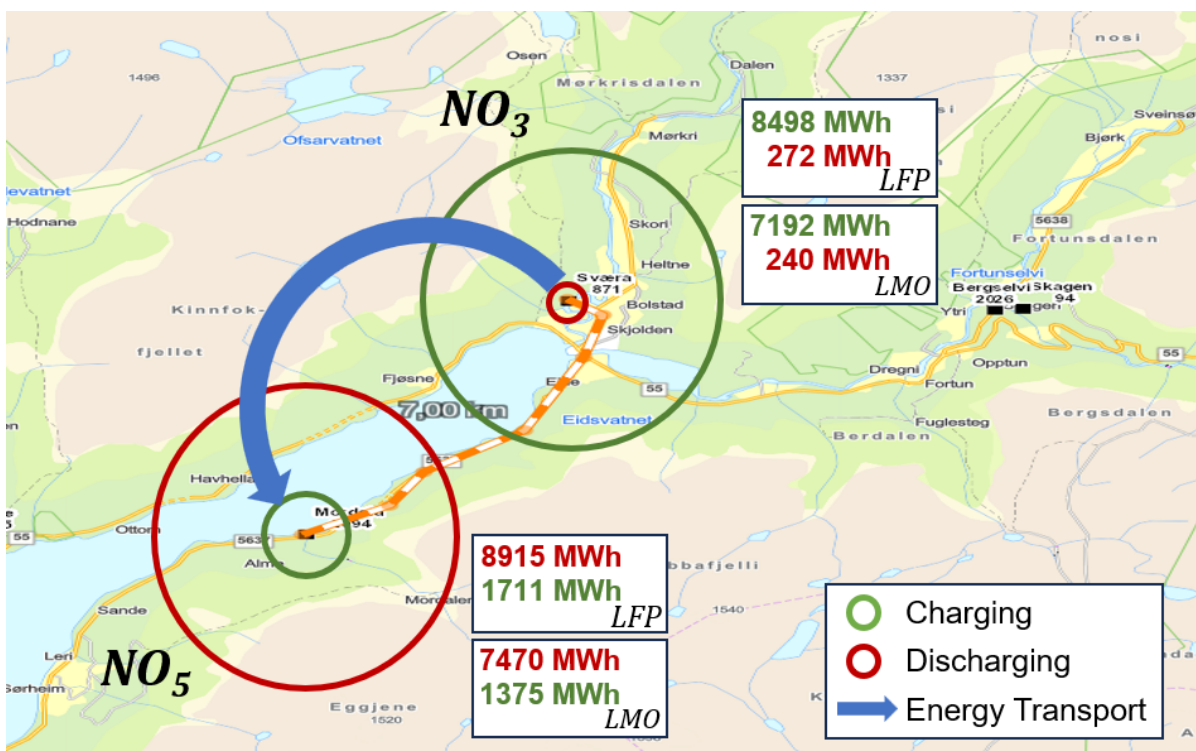


Figure 5.1: Charging, discharging, and energy transport direction of two PESSs between NO5 and NO3, base cases, entire life span

Additionally, it can be seen that throughout its lifetime, the LFP battery has processed more energy than the LMO battery in every bidding zone. This indicates that the LFP system has effectively transported more energy between different zones by road.

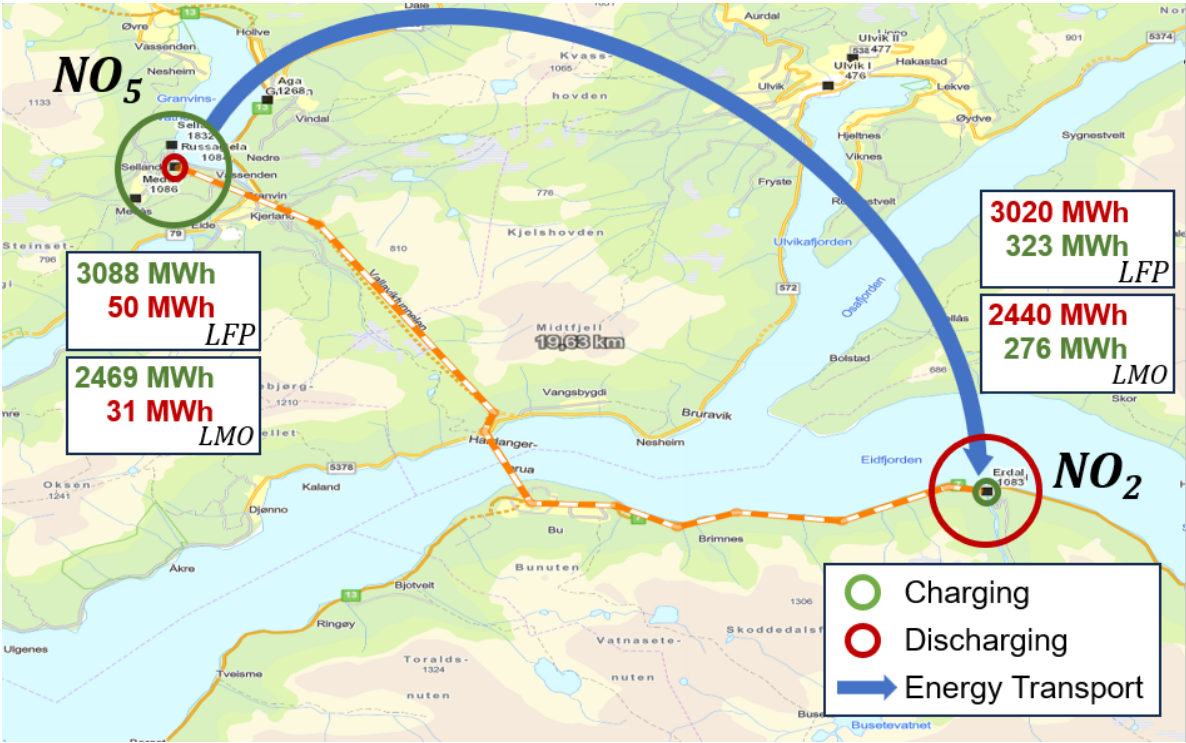


Figure 5.2: Charging, discharging, and energy transport direction of two PESSs between NO5 and NO2, base cases, entire life span

5.3.2. Daily Operation Pattern

Example days for the LFP battery are shown in Figure 5.3 and Figure 5.4. Both models effectively capture tariff valleys and peaks, aligning charging and discharging accordingly. The key difference lies in their operation strategies: the energy throughput model focuses solely on the price signal, leading to constant high-power operation during tariff peak and valley as in Figure 5.3a; while the semi-empirical model also considers DoD, resulting in a more conservative approach like shown in Figure 5.3b.

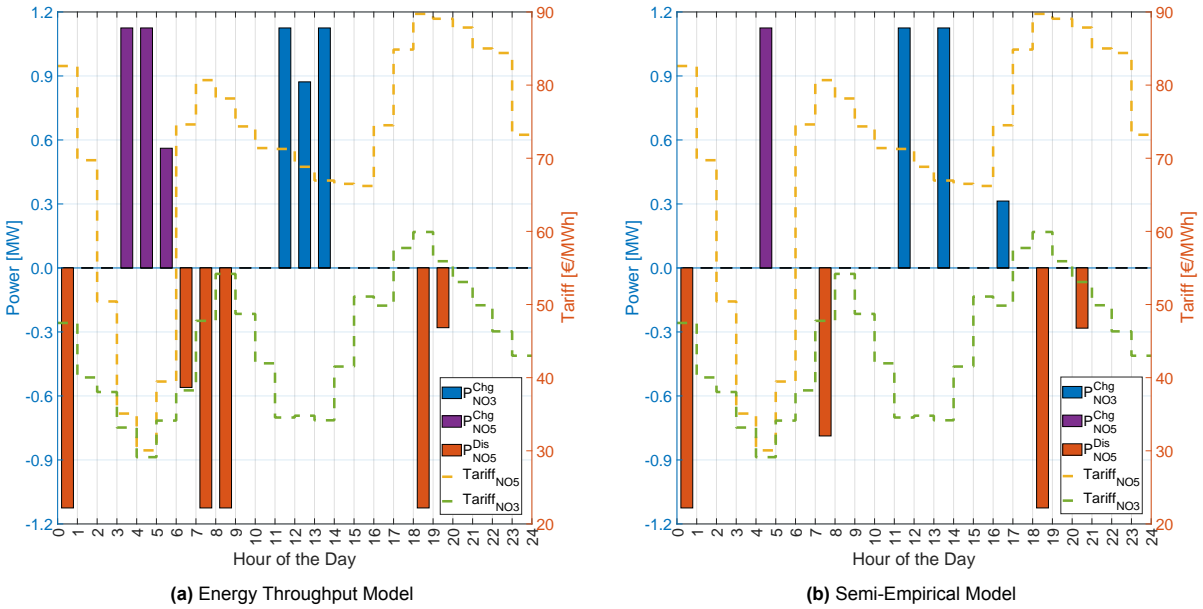


Figure 5.3: The charging/discharging power and hourly tariff of Feb 21, year 1, LFP battery

When tariffs are sufficiently lucrative to offset degradation costs, the semi-empirical model also operates at constant high power. As illustrated in Figure 5.4, the hourly tariffs in NO5, reaching around 250 €/MWh between 8-10 am and 4-6 pm, encourage both models to discharge at maximum power to maximize the profit.

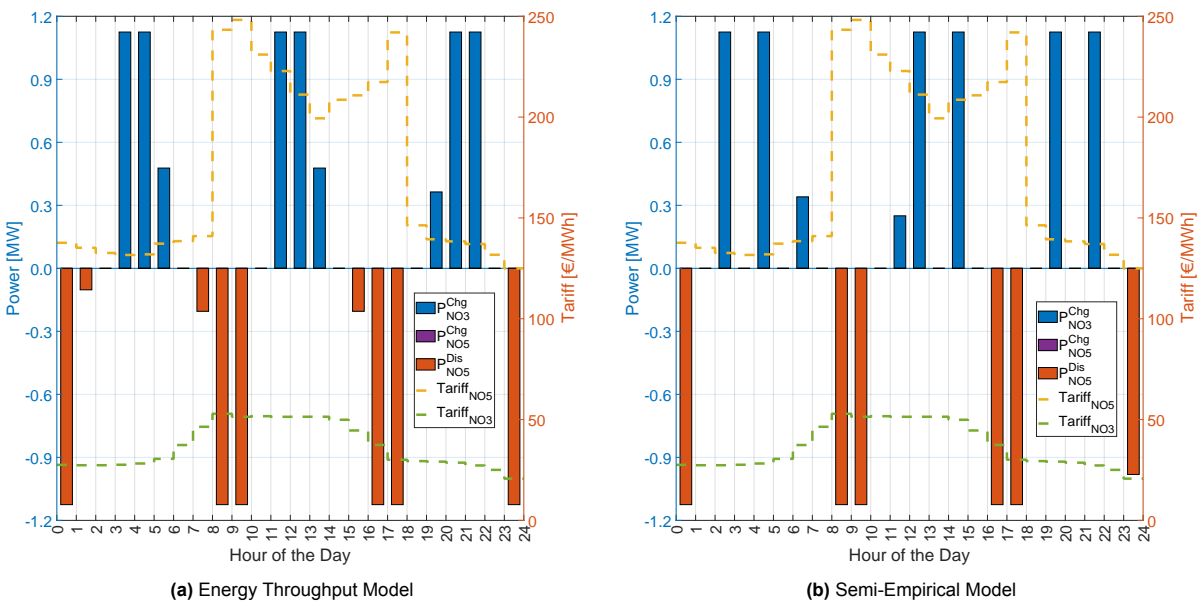


Figure 5.4: The charging/discharging power and hourly tariff of Jan 24, year 7, LFP battery

Examples days of LMO battery are depicted in Figure 5.5 and Figure 5.6. As shown in Figure 5.5, both models effectively capture the price valleys and peaks. However, in this instance, the energy throughput model operates the battery more conservatively compared to semi-empirical model. This conservative behavior arises because, although the €16/MWh throughput cost yields the highest lifetime NPV among energy throughput models, it tends to overestimate the degradation cost.

As indicated in Figure 3.8a, a €16/MWh cost corresponds to approximately 0.9 DoD; however, when the battery operates within a 0.2–0.5 DoD range, the degradation cost is below €9/MWh. Consequently, the semi-empirical model encourages the battery to align its operations with price peaks and valleys more frequently, while maintaining a preferable DoD to avoid excessive degradation due to high DoD.

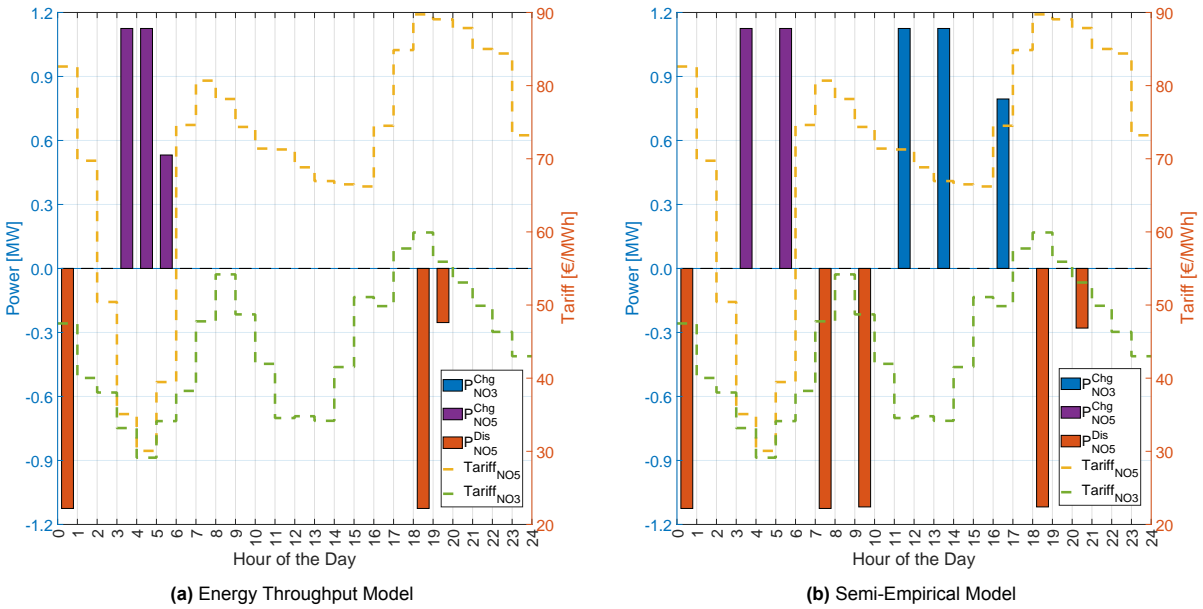


Figure 5.5: The charging/discharging power and hourly tariff of Feb 21, year 1, LMO battery

Similar to LFP battery, when the tariff is highly lucrative, the semi-empirical model also operates the battery at high DoD. As in Figure 5.6, when the price reaches approximately €250/MWh between 8 and 10 am, the battery discharges continuously at maximum power for 2 hours due to the high incentive.

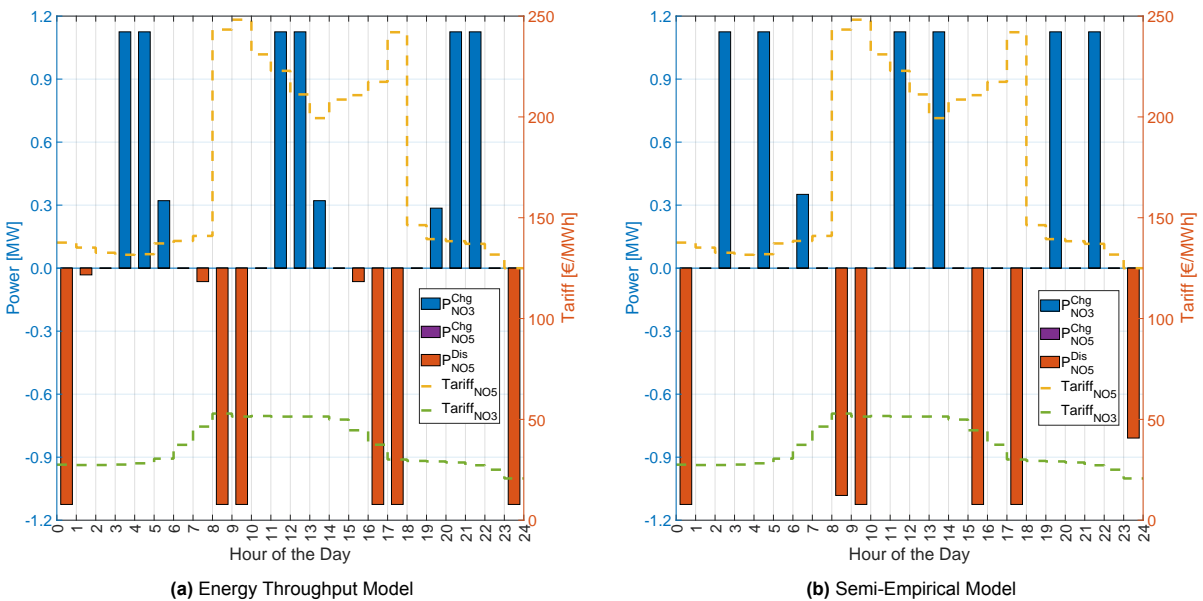


Figure 5.6: The charging/discharging power and hourly tariff of Jan 24, year 5, LMO battery

6

Future Work

In the previous chapters, several accelerated cases are discussed and research question 1 to 3 have been answered based on the simulation results.

While this study has provided insights into the profitability potential of portable energy storage systems and the impact of battery degradation models on battery optimization, several areas remain open for exploration in future research.

6.1. Multi-Layer Optimization

A potential direction for future research involves optimizing system profitability in conjunction with day-ahead electricity price prediction using a multi-layer optimization framework. The new framework will be expected to enhance the system profitability over an extended time horizon, such as a year or even the entire battery lifespan. This approach would require the incorporation of several objectives that were simplified in the current study:

6.1.1. System Location Planning

As previously discussed, the proposed PESS model does not account for long-term variations in electricity tariffs. Therefore, a system base relocation planning should be developed based on predicted price trends over an extended period to enhance system profitability.

6.1.2. State of Charge Level

The daily initial and final SoC level constraints will affect the system profitability by affecting daily charging/discharging opportunity and calendar aging. Thus, the proper selection of SoC levels is crucial.

6.1.3. SoH Stress Factor

In this study, the SOH stress factor S^{SoH} has a fixed upper limit value for simplicity. For higher profitability and to formulate the cyclic degradation term with higher precision, the upper limit of SOH stress factor S^{SoH} should be related to current battery health, too. The best S^{SoH} versus Equivalent Full Cycle Number N_{total} is yet to be derived.

6.1.4. Simulation Time Step

In this study, the simulation time step is one hour. A shorter time step offers higher flexibility for operation and potentially a higher profitability.

6.2. Service Portfolios

In this study, the battery solely engages in energy arbitrage within the Norwegian day-ahead market. Figure 6.1 illustrates the daily and monthly profits during the 3rd year of the semi-empirical LFP system. The data indicates that the proposed PESS achieves its highest profits in January and February, while

the lowest profits occur in June, July, October and April, showing negative values.

To enhance the profitability of the proposed system, integrating ancillary services such as contingency reserves, black-start regulation, and frequency regulation into the PESS portfolio is recommended. According to [60], combining revenues from various services is more profitable than relying solely on energy arbitrage.

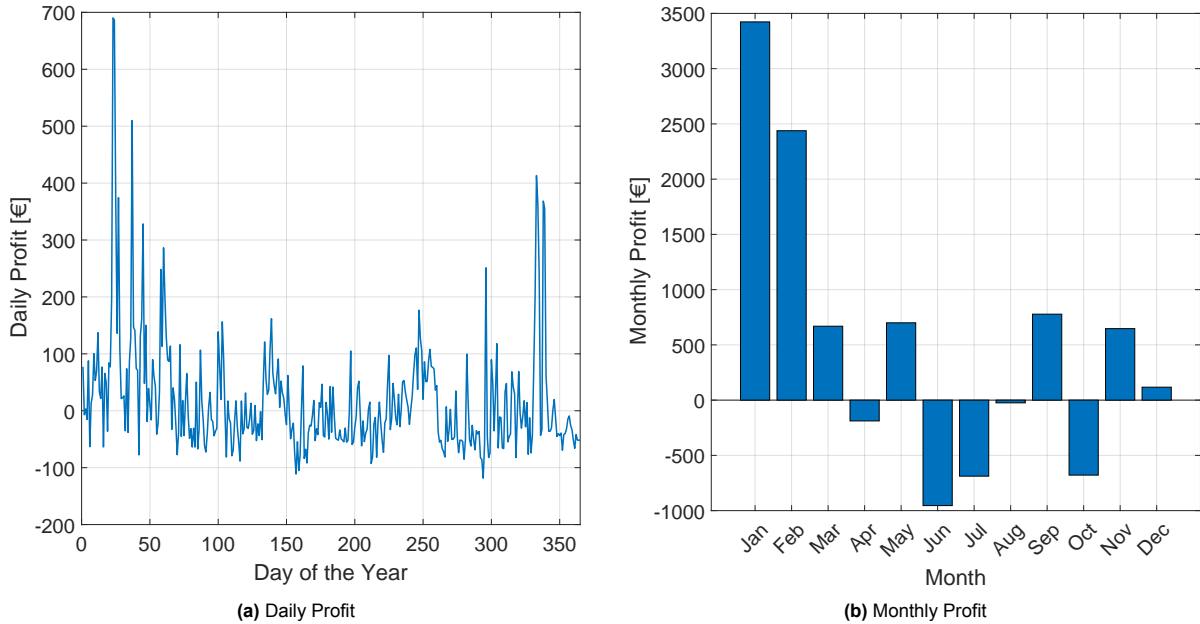


Figure 6.1: Daily and monthly profit of year 3 LFP battery with semi-empirical model

6.3. Price Prediction Error

This study assumes that the battery owner has a perfect day-ahead market (DAM) price forecast and successfully wins all bids throughout the battery's lifespan. However, in practice, perfect price forecasting is impossible, and the battery owner may not consistently win bids. As a result, there may be instances where the battery cannot be charged or discharged as scheduled, even when electricity prices are lucrative. Future research should address the impact of imperfect price predictions on system performance.

6.4. Grid Impact

While energy arbitrage offers potential financial benefits, it is essential to consider its impact on grid operations, transmission constraints, and environmental implications to ensure that it supports broader energy system goals. In this study, the portable energy storage system is essentially transporting electricity through highway instead of cables. To see if the system can have a positive grid impact, for example, help address congestion; a network energy flow simulation could be run and compared to the energy transmission by the PESS in this study.

6.5. Degradation Model

6.5.1. Different Stress Factors

Battery degradation is influenced by various factors, including depth of discharge (DoD), average state of charge (SoC), and temperature. Incorporating these multiple stress factors into the analysis enhances the precision of capturing battery degradation, thereby providing a more accurate predictive model.

6.5.2. Cycle Counting Algorithm

In this study, an online cycle counting algorithm is used to count the half charging/discharging cycles. For improved accuracy, future studies could implement the rainflow cycle-counting algorithm, which differentiates between half and full cycles, along with a revised objective function formulation as referenced in [57]. The relative error between rainflow cycle-counting and online cycle-counting algorithm is compared in [59].

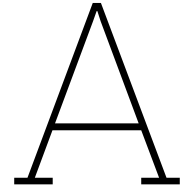
References

- [1] S.Osaka. *Earth breached a feared level of warming over the past year. Are we doomed?* 2024. URL: <https://www.washingtonpost.com/climate-environment/2024/02/08/1-5-celsius-global-warming-record/>.
- [2] M.Henriques. *Climate change: The 1.5C threshold explained.* 2024. URL: <https://www.bbc.com/future/article/20231130-climate-crisis-the-15c-global-warming-threshold-explained>.
- [3] Max Roser. “The world’s energy problem”. In: *Our World in Data* (2020). URL: <https://ourworldindata.org/worlds-energy-problem>.
- [4] Hannah Ritchie and Pablo Rosado. “Fossil fuels”. In: *Our World in Data* (2017). URL: <https://ourworldindata.org/fossil-fuels>.
- [5] International Energy Agency. *Renewables 2023*. IEA, Paris. Licence: CC BY 4.0. 2024. URL: <https://www.iea.org/reports/renewables-2023>.
- [6] Hannah Ritchie, Max Roser, and Pablo Rosado. “Renewable Energy”. In: *Our World in Data* (2020). URL: <https://ourworldindata.org/renewable-energy>.
- [7] Paul Denholm et al. “The Role of Energy Storage with Renewable Electricity Generation”. In: (Jan. 2010). DOI: 10.2172/972169.
- [8] Abbas A. Akhil et al. “DOE/EPRI Electricity Storage Handbook in Collaboration with NRECA”. In: (Sept. 2016). DOI: 10.2172/1431469. URL: <https://www.osti.gov/biblio/1431469>.
- [9] European Parliament and Council. *Directive (EU) 2019/944 on Common Rules for the Internal Market for Electricity and Amending Directive 2012/27/EU*. <https://eur-lex.europa.eu/legal-content/EN/TXT/?uri=CELEX:32019L0944>. Accessed: 2024-05-21. 2019.
- [10] Bolun Xu et al. “A comparison of policies on the participation of storage in U.S. frequency regulation markets”. In: *2016 IEEE Power and Energy Society General Meeting (PESGM)*. 2016, pp. 1–5. DOI: 10.1109/PESGM.2016.7741531.
- [11] Richard Schmalensee. “Strengths and weaknesses of traditional arrangements for electricity supply”. In: *Handbook on Electricity Markets*. Edward Elgar Publishing, Nov. 2021. ISBN: 9781788979955. DOI: 10.4337/9781788979955.00008.
- [12] Kyle Bradbury, Lincoln Pratson, and Dalia Patiño-Echeverri. “Economic viability of energy storage systems based on price arbitrage potential in real-time U.S. electricity markets”. In: *Applied Energy* 114 (2014), pp. 512–519. ISSN: 0306-2619. DOI: <https://doi.org/10.1016/j.apenergy.2013.10.010>. URL: <https://www.sciencedirect.com/science/article/pii/S0306261913008301>.
- [13] Boqiang Lin and Wei Wu. “Economic viability of battery energy storage and grid strategy: A special case of China electricity market”. In: *Energy* 124 (2017), pp. 423–434. ISSN: 0360-5442. DOI: <https://doi.org/10.1016/j.energy.2017.02.086>. URL: <https://www.sciencedirect.com/science/article/pii/S0360544217302682>.
- [14] Dennis Metz and João Tomé Saraiva. “Use of battery storage systems for price arbitrage operations in the 15- and 60-min German intraday markets”. In: *Electric Power Systems Research* 160 (2018), pp. 27–36. ISSN: 0378-7796. DOI: <https://doi.org/10.1016/j.epsr.2018.01.020>. URL: <https://www.sciencedirect.com/science/article/pii/S0378779618300282>.
- [15] Yu Hu, Miguel Armada, and María Jesús Sánchez. “Potential utilization of battery energy storage systems (BESS) in the major European electricity markets”. In: *Applied Energy* 322 (2022), p. 119512. ISSN: 0306-2619. DOI: <https://doi.org/10.1016/j.apenergy.2022.119512>. URL: <https://www.sciencedirect.com/science/article/pii/S0306261922008340>.

- [16] Ángel Arcos-Vargas, David Canca, and Fernando Núñez. “Impact of battery technological progress on electricity arbitrage: An application to the Iberian market”. In: *Applied Energy* 260 (2020), p. 114273. ISSN: 0306-2619. DOI: <https://doi.org/10.1016/j.apenergy.2019.114273>. URL: <https://www.sciencedirect.com/science/article/pii/S0306261919319609>.
- [17] Weiqi Zhang and Victor M. Zavala. “Remunerating space–time, load-shifting flexibility from data centers in electricity markets”. In: *Applied Energy* 326 (2022), p. 119930. ISSN: 0306-2619. DOI: <https://doi.org/10.1016/j.apenergy.2022.119930>. URL: <https://www.sciencedirect.com/science/article/pii/S0306261922011874>.
- [18] Clay T. Elmore and Alexander W. Dowling. “Learning spatiotemporal dynamics in wholesale energy markets with dynamic mode decomposition”. In: *Energy* 232 (2021), p. 121013. ISSN: 0360-5442. DOI: <https://doi.org/10.1016/j.energy.2021.121013>. URL: <https://www.sciencedirect.com/science/article/pii/S0360544221012615>.
- [19] Jason Mann and Ljubo Mitrasevic. *Nodal pricing in GB: Brief overview of conclusions and impact on use of flexibility resources*. Presentation at Strommarkttreffen. 2023. URL: [https://www.strommarkttreffen.org/05_Jason%20Mann%20and%20Ljubo%20Mitrasevic%20\(FTI%20Consulting\)%20Cost-Benefit-Analysis%20of%20moving%20to%20zonal%20or%20nodal%20electricity%20market%20design%20in%20GB.pdf](https://www.strommarkttreffen.org/05_Jason%20Mann%20and%20Ljubo%20Mitrasevic%20(FTI%20Consulting)%20Cost-Benefit-Analysis%20of%20moving%20to%20zonal%20or%20nodal%20electricity%20market%20design%20in%20GB.pdf).
- [20] CAISO. *Price Map*. <http://www.caiso.com/PriceMap/Pages/default.aspx>. Accessed: 2024-05-25.
- [21] B. Tepe et al. “Analysis of optimally composed EV pools for the aggregated provision of frequency containment reserve and energy arbitrage trading”. In: *5th E-Mobility Power System Integration Symposium (EMOB 2021)*. Vol. 2021. 2021, pp. 175–180. DOI: 10.1049/icp.2021.2521.
- [22] Mushfiqur R. Sarker, Daniel Julius Olsen, and Miguel A. Ortega-Vazquez. “Co-Optimization of Distribution Transformer Aging and Energy Arbitrage Using Electric Vehicles”. In: *IEEE Transactions on Smart Grid* 8.6 (2017), pp. 2712–2722. DOI: 10.1109/TSG.2016.2535354.
- [23] Guannan He et al. “Utility-Scale Portable Energy Storage Systems”. In: *Joule* 5.2 (2021), pp. 379–392. ISSN: 2542-4351. DOI: <https://doi.org/10.1016/j.joule.2020.12.005>. URL: <https://www.sciencedirect.com/science/article/pii/S2542435120305730>.
- [24] G. Antonopoulos et al. *Nodal Pricing in the European Internal Electricity Market*. Publications Office of the European Union, 2020. ISBN: 978-92-76-17571-1. DOI: 10.2760/41018.
- [25] *Zonal versus Nodal Electricity Pricing: The PJM Experience*. <https://fsr.eui.eu/zonal-versus-nodal-electricity-pricing-the-pjm-experience/>. Interview by FSR. Feb. 2019.
- [26] NordPool. *Price Map*. Accessed: 2024-05-25. URL: <https://data.nordpoolgroup.com/map?deliveryDate=latest¤cy=EUR&market=DayAhead&mapDataType=Price&resolution=60>.
- [27] Andrés F. Peñaranda, David Romero-Quete, and Camilo A. Cortés. “Grid-Scale Battery Energy Storage for Arbitrage Purposes: A Colombian Case”. In: *Batteries* 7.3 (2021). ISSN: 2313-0105. DOI: 10.3390/batteries7030059. URL: <https://www.mdpi.com/2313-0105/7/3/59>.
- [28] Yunfei Bai, Jihong Wang, and Wei He. “Energy arbitrage optimization of lithium-ion battery considering short-term revenue and long-term battery life loss”. In: *Energy Reports* 8 (2022). Selected papers from 2022 7th International Conference on Advances on Clean Energy Research, pp. 364–371. ISSN: 2352-4847. DOI: <https://doi.org/10.1016/j.egy.2022.10.209>. URL: <https://www.sciencedirect.com/science/article/pii/S235248472202145X>.
- [29] Xin Jiang et al. “Optimal configuration of grid-side battery energy storage system under power marketization”. In: *Applied Energy* 272 (2020), p. 115242. ISSN: 0306-2619. DOI: <https://doi.org/10.1016/j.apenergy.2020.115242>. URL: <https://www.sciencedirect.com/science/article/pii/S0306261920307546>.
- [30] Bolun Xu et al. “BESS Control Strategies for Participating in Grid Frequency Regulation”. In: *IFAC Proceedings Volumes* 47.3 (2014). 19th IFAC World Congress, pp. 4024–4029. ISSN: 1474-6670. DOI: <https://doi.org/10.3182/20140824-6-ZA-1003.02148>. URL: <https://www.sciencedirect.com/science/article/pii/S1474667016422329>.

- [31] Marco Stecca et al. "Lifetime Estimation of Grid-Connected Battery Storage and Power Electronics Inverter Providing Primary Frequency Regulation". In: *IEEE Open Journal of the Industrial Electronics Society* 2 (2021), pp. 240–251. DOI: 10.1109/OJIES.2021.3064635.
- [32] Pietro Elia Campana et al. "Li-ion batteries for peak shaving, price arbitrage, and photovoltaic self-consumption in commercial buildings: A Monte Carlo Analysis". In: *Energy Conversion and Management* 234 (2021), p. 113889. ISSN: 0196-8904. DOI: <https://doi.org/10.1016/j.enconman.2021.113889>. URL: <https://www.sciencedirect.com/science/article/pii/S0196890421000662>.
- [33] Wiljan Vermeer, Gautham Ram Chandra Mouli, and Pavol Bauer. "A Comprehensive Review on the Characteristics and Modeling of Lithium-Ion Battery Aging". In: *IEEE Transactions on Transportation Electrification* 8.2 (2022), pp. 2205–2232. DOI: 10.1109/TTE.2021.3138357.
- [34] Yang Li et al. "Model Order Reduction Techniques for Physics-Based Lithium-Ion Battery Management: A Survey". In: *IEEE Industrial Electronics Magazine* 16.3 (2022), pp. 36–51. DOI: 10.1109/MIE.2021.3100318.
- [35] Johannes Schmalstieg et al. "A holistic aging model for Li(NiMnCo)O₂ based 18650 lithium-ion batteries". In: *Journal of Power Sources* 257 (2014), pp. 325–334. ISSN: 0378-7753. DOI: <https://doi.org/10.1016/j.jpowsour.2014.02.012>. URL: <https://www.sciencedirect.com/science/article/pii/S0378775314001876>.
- [36] Sergio J. Navas et al. "Modelling Li-ion batteries using equivalent circuits for renewable energy applications". In: *Energy Reports* 9 (2023), pp. 4456–4465. ISSN: 2352-4847. DOI: <https://doi.org/10.1016/j.egy.2023.03.103>. URL: <https://www.sciencedirect.com/science/article/pii/S2352484723003414>.
- [37] MathWorks. *Battery Equivalent Circuit*. <https://nl.mathworks.com/help/simscape-battery/ref/batteryequivalentcircuit.html>. Accessed: 2024-06-06.
- [38] S. Nejad, D.T. Gladwin, and D.A. Stone. "A systematic review of lumped-parameter equivalent circuit models for real-time estimation of lithium-ion battery states". In: *Journal of Power Sources* 316 (2016), pp. 183–196. ISSN: 0378-7753. DOI: <https://doi.org/10.1016/j.jpowsour.2016.03.042>. URL: <https://www.sciencedirect.com/science/article/pii/S0378775316302427>.
- [39] Jingwen Wei, Guangzhong Dong, and Zonghai Chen. "Remaining Useful Life Prediction and State of Health Diagnosis for Lithium-Ion Batteries Using Particle Filter and Support Vector Regression". In: *IEEE Transactions on Industrial Electronics* 65.7 (2018), pp. 5634–5643. DOI: 10.1109/TIE.2017.2782224.
- [40] Junchuan Shi, Alexis Rivera, and Dazhong Wu. "Battery health management using physics-informed machine learning: Online degradation modeling and remaining useful life prediction". In: *Mechanical Systems and Signal Processing* 179 (2022), p. 109347. ISSN: 0888-3270. DOI: <https://doi.org/10.1016/j.ymsp.2022.109347>. URL: <https://www.sciencedirect.com/science/article/pii/S0888327022004824>.
- [41] Feng Wang, Ziliang Zhai, Zhen Zhao, et al. "Physics-informed neural network for lithium-ion battery degradation stable modeling and prognosis". In: *Nature Communications* 15 (2024), p. 4332. DOI: 10.1038/s41467-024-48779-z. URL: <https://www.nature.com/articles/s41467-024-48779-z>.
- [42] Bolun Xu et al. "Modeling of Lithium-Ion Battery Degradation for Cell Life Assessment". In: *IEEE Transactions on Smart Grid* 9.2 (2018), pp. 1131–1140. DOI: 10.1109/TSG.2016.2578950.
- [43] M. Schimpe et al. "Comprehensive Modeling of Temperature-Dependent Degradation Mechanisms in Lithium Iron Phosphate Batteries". In: *Journal of The Electrochemical Society* 165.2 (Jan. 2018), A181. DOI: 10.1149/2.1181714jes. URL: <https://dx.doi.org/10.1149/2.1181714jes>.
- [44] Alan Millner. "Modeling Lithium Ion battery degradation in electric vehicles". In: *2010 IEEE Conference on Innovative Technologies for an Efficient and Reliable Electricity Supply*. 2010, pp. 349–356. DOI: 10.1109/CITRES.2010.5619782.

- [45] Izaro Laresgoiti et al. “Modeling mechanical degradation in lithium ion batteries during cycling: Solid electrolyte interphase fracture”. In: *Journal of Power Sources* 300 (2015), pp. 112–122. ISSN: 0378-7753. DOI: <https://doi.org/10.1016/j.jpowsour.2015.09.033>. URL: <https://www.sciencedirect.com/science/article/pii/S0378775315302949>.
- [46] Milton A. Miner. “Cumulative Damage in Fatigue”. In: *Journal of Applied Mechanics* 12.3 (Mar. 2021), A159–A164. ISSN: 0021-8936. DOI: 10.1115/1.4009458. eprint: https://asmedigitalcollection.asme.org/appliedmechanics/article-pdf/12/3/A159/6745060/a159_1.pdf. URL: <https://doi.org/10.1115/1.4009458>.
- [47] M. Broussely et al. “Main aging mechanisms in Li ion batteries”. In: *Journal of Power Sources* 146.1 (2005). Selected papers presented at the 12th International Meeting on Lithium Batteries, pp. 90–96. ISSN: 0378-7753. DOI: <https://doi.org/10.1016/j.jpowsour.2005.03.172>. URL: <https://www.sciencedirect.com/science/article/pii/S0378775305005082>.
- [48] Matthieu Dubarry, Nan Qin, and Paul Brooker. “Calendar aging of commercial Li-ion cells of different chemistries – A review”. In: *Current Opinion in Electrochemistry* 9 (2018), pp. 106–113. ISSN: 2451-9103. DOI: <https://doi.org/10.1016/j.coelec.2018.05.023>. URL: <https://www.sciencedirect.com/science/article/pii/S2451910318300929>.
- [49] Xin Sui et al. “The Degradation Behavior of LiFePO₄/C Batteries during Long-Term Calendar Aging”. In: *Energies* 14.6 (2021). ISSN: 1996-1073. DOI: 10.3390/en14061732. URL: <https://www.mdpi.com/1996-1073/14/6/1732>.
- [50] Akram Eddahech, Olivier Briat, and Jean-Michel Vinassa. “Performance comparison of four lithium-ion battery technologies under calendar aging”. In: *Energy* 84 (2015), pp. 542–550. ISSN: 0360-5442. DOI: <https://doi.org/10.1016/j.energy.2015.03.019>. URL: <https://www.sciencedirect.com/science/article/pii/S0360544215003138>.
- [51] Daniel-Ioan Stroe et al. “Degradation Behavior of Lithium-Ion Batteries During Calendar Ageing—The Case of the Internal Resistance Increase”. In: *IEEE Transactions on Industry Applications* 54.1 (2018), pp. 517–525. DOI: 10.1109/TIA.2017.2756026.
- [52] Kailong Liu et al. “Gaussian Process Regression With Automatic Relevance Determination Kernel for Calendar Aging Prediction of Lithium-Ion Batteries”. In: *IEEE Transactions on Industrial Informatics* 16.6 (2020), pp. 3767–3777. DOI: 10.1109/TII.2019.2941747.
- [53] Alfen. *The Battery MOBILE X Data Sheet*. <https://alfen.com/thebattery-mobile>. June 2023.
- [54] ENTSO-E. *Day-ahead Prices*. 2023. URL: <https://transparency.entsoe.eu/>.
- [55] Velju. *European Countries With The Highest Truck Driver Salaries*. 2023. URL: <https://velju.com/logistic-job-description/driver/truck-driver-salaries-eu/>.
- [56] Yuanyuan Shi et al. “A Convex Cycle-based Degradation Model for Battery Energy Storage Planning and Operation”. In: *2018 Annual American Control Conference (ACC)*. 2018, pp. 4590–4596. DOI: 10.23919/ACC.2018.8431814.
- [57] Yuanyuan Shi et al. “Optimal Battery Control Under Cycle Aging Mechanisms in Pay for Performance Settings”. In: *IEEE Transactions on Automatic Control* 64.6 (2019), pp. 2324–2339. DOI: 10.1109/TAC.2018.2867507.
- [58] Stephen Boyd and Lieven Vandenbergh. *Convex Optimization*. Cambridge University Press, 2004.
- [59] Riccardo Nebuloni et al. “A Real-Time Cycle Counting Method for Battery Degradation Calculation in MILP Models”. In: *2023 IEEE International Conference on Environment and Electrical Engineering and 2023 IEEE Industrial and Commercial Power Systems Europe (EEEIC / I&CPS Europe)*. 2023, pp. 1–6. DOI: 10.1109/EEEIC/ICPSEurope57605.2023.10194776.
- [60] Luca Argiolas et al. “Optimal Battery Energy Storage Dispatch in Energy and Frequency Regulation Markets While Peak Shaving an EV Fast Charging Station”. In: *IEEE Open Access Journal of Power and Energy* 9 (2022), pp. 374–385. DOI: 10.1109/OAJPE.2022.3198553.



Supplemental Results

Table A.1: Energy throughput model simulation results with different degradation cost values, LFP battery

Degradation Cost [€/MWh]	Service Life [day]	Pay-Back Period [day]	Lifetime Revenue [€]	Ner Present Value [€]	Investment Cost [€]	Investment Return Rate
12	2,215	1,871	588,726	654,799	596,400	9.79%
14	2,329	1,954	600,5584	660,658	596,400	10.77%
16	2,483	2,076	603,333	658,607	596,400	10.43%
18	2,668	2,267	610,226	651,806	596,400	9.29%
20	2,974	2,623	609,792	635,703	596,400	6.59%

Table A.2: Energy throughput model simulation results with different degradation cost values, LMO battery

Degradation Cost [€/MWh]	Service Life [day]	Pay-Back Period [day]	Lifetime Revenue [€]	Ner Present Value [€]	Investment Cost [€]	Investment Return Rate
14	1,503	-	385,456	502,744	506,400	-
16	1,610	1,605	393,839	507,569	506,400	0.23%
18	1,750	1,742	396,052	507,048	506,400	0.13%
20	1,980	-	406,292	503,439	506,400	-
22	2,251	-	408,475	492,668	506,400	-

Table A.3: Energy throughput model simulation results of stationary battery system in different bidding zone, LFP battery

Battery Chemistry	Degradation Cost [€/MWh]	Bidding Zone	Service Life [day]	Lifetime Revenue [€]	Net Present Value [€]	Investment Cost [€]	Break Even?
LFP	14	NO1	5,394	297,166	263,475	534,000	no
		NO2	4,755	341,589	305,883	534,000	no
		NO3	6,485	174,693	162,790	534,000	no
		NO4	7,129	111,627	114,215	534,000	no
		NO5	5,499	246,699	223,713	534,000	no

Table A.4: Energy throughput model simulation results of stationary battery system in different bidding zone, LMO battery

Battery Chemistry	Degradation Cost [€/MWh]	Bidding Zone	Service Life [day]	Lifetime Revenue [€]	Net Present Value [€]	Investment Cost [€]	Break Even?
LMO	16	NO1	4,424	263,434	255,307	444,000	no
		NO2	3,897	278,565	279,450	444,000	no
		NO3	5,665	165,283	166,011	444,000	no
		NO4	6,524	108,238	118,924	444,000	no
		NO5	4,731	210,544	213,578	444,000	no

Acknowledgement

I would like to conclude this thesis by expressing my gratefulness to all those who have supported me throughout the journey of completing my thesis. Their support, guidance and encouragement are my most valuable motivation all the way. Without them, this thesis would still remain an preliminary idea.

First of all, I would like to express my sincere gratitude to my primary supervisor from Delft University of Technology, Dr. Zian Qin, who gave me the opportunity to pursue my thesis in the field of batteries a year ago, a field I knew nothing about at the time. His encouragement and insightful feedback have been essential throughout the entire research process, and as I look back at the end of this thesis, I want to share this joy with him. Additionally, I am also thankful to Dr. Hani Vahedi and Dr. Pedro Vergara Barrios for agreeing to be on the thesis committee.

I am also indebted to my company supervisor, René van Wesenbeeck, from Alfen. During my year in Alfen, he has given me guidance and freedom to explore the battery field with a creative and holistic mindset. With his help, I was quickly integrated into the R&D department, where I got to meet all my wonderful colleagues. I have felt their support both inside and outside the office and I must say thank you all for your professional advice on my work and for being such great listeners to my ideas. The collaborative environment in Alfen has been an inspiration and a driving force behind the completion of this thesis.

I also want to extend my heartfelt thanks to my friends, for their unwavering support and trust. They were more than willing to share their knowledge and help me along the way without hesitation. I feel incredibly fortunate for the bond we have formed. The time we spent together is unforgettable and our friendship will always be cherished.

Last but not least, I am deeply grateful to my parents. Their belief in me has lifted my spirits and motivated me. Their selfless devotion is a constant reminder to me to be a better person. I cannot express my gratitude to them enough for giving me the privilege of this life-changing experience at Delft University of Technology.

*Xiangyu Wang
Delft, August 2024*